Southern African Large Telescope

Title:	**RSS Commissioning Tasks Report**
Author(s):	**Anja C. Schröder, Steve M. Crawford, & the SALT team**
Doc. number:	**2202AA0001**
Version:	**1**
Date:	*22 May 2014*
Keywords:	RSS commissioning
Approved:	**David Buckley (Ast Ops Manager)**

Signature:_____ Date:_____

ABSTRACT

This report on the RSS commissioning tasks is a summary of the information and reports listed on the SALT wiki page on RSS Science Commissioning. Various people have contributed to the reports. This first draft includes all tasks (except Fabry-Perot tasks which will presented in a separate document) of 'very high' and 'high' priorities and a selection of 'medium' and 'low' priorities.

South African Astronomical Observatory, Cape Town 7925, South Africa

Contents

1 Introduction

For the RSS commissioning, a series of tasks was compiled by Ken Nordsieck which test and characterize the instrument in four modes: (i) imaging (identifier 'IMG'), (ii) longslit (identifier 'LS'), (iii) multiobject spectroscopy (identifier 'MOS'), and (iv) Fabry-Perot (identifier 'FP'). These tasks are listed on a SALT wiki webpage[1] together with the details of the tasks, their results and any associated reports.

At the time of this draft, all 'very high' and 'high' priority tasks were done and included in this report, except for the Fabry-Perot tasks which will be discussed in a separate document. Some of the 'medium' and 'low' priority cases were also added. The tasks are sorted by priority and very much as they appear on the full wiki list (for example, tasks added later at the bottom of the table are an exception). The numbering of the tasks on that wiki page is given in brackets in the section title for easier cross-reference.

Some of the links and publications useful for understanding the RSS instrument and its commissioning are:

- Burgh et al, 2003, The Prime Focus Imaging Spectrograph for the Southern African Large Telescope: optical design
- Kobulnicky et al 2003, The Prime Focus Imaging Spectrograph for the Southern African Large Telescope: operational modes
- The Wisconsin RSS page: http://www.sal.wisc.edu/PFIS/
- RSS section the Call for Proposal: http://pysalt.salt.ac.za/proposal_calls/current/ProposalCall.html#h.7u21mjj3yi9u
- List of RSS publications: http://www.salt.ac.za/science/publications/
- Science wiki Data Quality page: https://sciencewiki.salt.ac.za/index.php/Data_Quality#RSS

2 Bias frames (Task #1)

Task: To determine the usefulness and stability of bias frames with different instrument settings.

Data: I have used all master bias files for January 2013 plus 1st and 2nd February. They are made with a variety of settings, see Table 1 for details. Masks, filters and observing modes varied. Here is an overview of the settings:

- 17 bias files with CCDSUM = 2x2; eight with 4x4, and one with 2x4.
- 2 bias files have GAINSET = bright (BR) and ROSPEED = fast (FA); 2 have faint (FA) and fast, and the rest have faint and slow (SL).
- Usually the master bias is made of 11 individual bias frames. There are 5 exceptions to this: in one case there were only 10 bias frames available, in one case 12 were used, in two cases 22 were used, and in one case 33.

Table 1: Details of bias frame observations.

Date	CCDSUM	GAINSET/ ROSPEED	number of images	exposure numbers	characteristics	explanation
20130102	2x2	FASL	11	003 - 013		
20130103	2x2	BRFA	11	013 - 023	noisy	fast readout
20130104	2x2	FASL	11	014 - 024		
20130105	2x2	FASL	11	009 - 019		
20130106	2x2	FASL	11	041 - 051		
20130107	2x2	FASL	11	102 - 112		
20130107	4x4	BRFA	11	113 - 123	noisy (fishbone pattern)	fast readout
20130107	4x4	FASL	11	148 - 158		
20130108	2x2	FASL	11	009 - 019		
20130112	4x4	FAFA	33	001 - 033	noisy (fishbone pattern), gradient	fast readout
20130112	2x2	FASL	22	034 - 055	noisy (faint fishbone pattern on ext 5/6)	problem with saltcombine
20130113	2x2	FASL	11	056 - 066		
20130113	2x4	FASL	11	067 - 077		
20130113	4x4	FAFA	11	078 - 088	noisy (fishbone pattern)	fast readout
20130113	4x4	FASL	11	089 - 099		
20130123	4x4	FASL	22	001 - 022		
20130124	2x2	FASL	11	009 - 019	gradient	
20130125	2x2	FASL	11	072 - 082	stripes	
20130126	2x2	FASL	11	049 - 059		
20130127	2x2	FASL	10	020 - 029	stripes	
20130128	2x2	FASL	11	030 - 040		
20130131	2x2	FASL	11	001 - 011	stripes	
20130131	4x4	FASL	11	101 - 111		
20130201	2x2	FASL	15	001 - 004, 011 - 022	strong gradient, noisy	problem with saltcombine
20130202	2x2	FASL	12	084 - 095	noisy	problem with saltcombine
20130202	4x4	FASL	11	096 - 106		

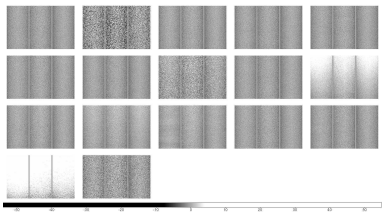

(a) The image for 2x2 bias frames shows the full frames in order of dates: 102, 103 (BRFA), 104, 105, 106, 107, 108, 112, 113, 124, 125, 126, 127, 128, 131, 201, 202.

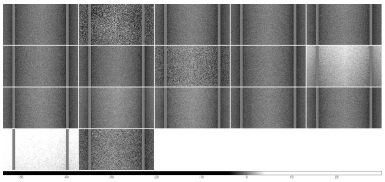

(b) This image of the 2x2 bias frames shows a zoom-in onto the centre part of the middle CCD in order of dates: 102, 103 (BRFA), 104, 105, 106, 107, 108, 112, 113, 124, 125, 126, 127, 128, 131, 201, 202.

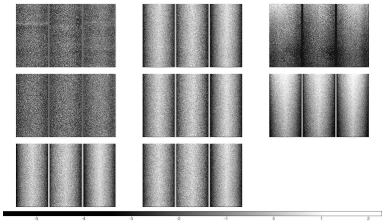

(c) The image of the 4x4 bias frames shows the full frames in order of dates: 107 (BRFA), 107, 112 (FAFA), 113 (FAFA), 113, 123, 131, 202.

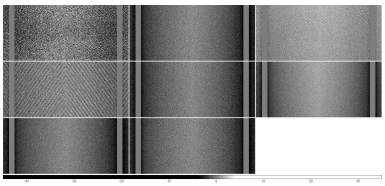

(d) This image of the 4x4 bias frames shows a zoom-in onto the centre part of the middle CCD in order of dates: 107 (BRFA), 107, 112 (FAFA), 113 (FAFA), 113, 123, 131, 202.

Figure 1

Also given in the table are obvious problems with the master bias images and their possible explanations. These are discussed in detail below.

Data reduction: All images were visually inspected. The IRAF task `imexam` was used with `nclip=3` (to avoid hot pixels and cosmic rays) to get statistics on each extension (excluding a rim of 2 – 4 pixels at the edges of the image).

Analysis: Inspecting the master images visually shows immediately that the FASL settings give the smoothest images, while the other settings are noisier and often show a fishbone pattern (note that in case of the 20130112 image with 2x2 (FASL) a fishbone pattern appears faintly on extensions 5 and 6 as well). Figure 1 shows the images from left to right, top to bottom in order of date.

Figure 2 shows the statistical mean values (left) and standard deviation (right) per extension (amplifier; coded by colour) versus date (days counted consecutively) for 2x2 frames (top panel) and 4x4 frames (bottom panel). The FASL images are connected by a line (per extension). It is obvious that

- Each CCD shows the same horizontal variation (*i.e.*, brighter in the middle, dimmer at the edges).
- The BRFA and FAFA images do not follow the pattern of the FASL images.
- Images with a gradient (112-FAFA, 123-FASL, 0124, 0201) show a significantly higher mean. The standard deviation n case of 2x2 frames (0124, 0201) are also higher, while for the 4x4

[1] http://wiki.salt.ac.za/index.php/RSS_Science_Commissioning

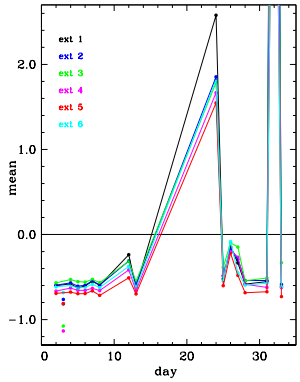

(a) Mean counts per extension for 2x2 bias frames. The date 0201 lies outside the plot limits (at 7−15 counts).

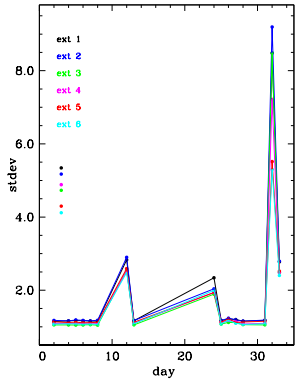

(b) Standard deviation per extension for 2x2 bias frames.

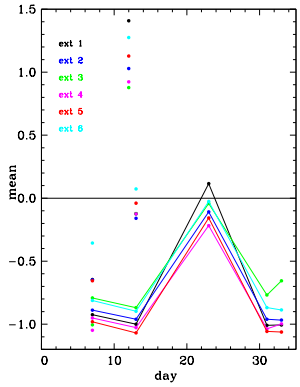

(c) Mean counts per extension for 4x4 bias frames.

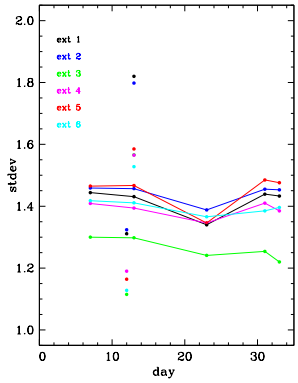

(d) Standard deviation per extension for 4x4 bias frames. The values for BRFA (date 0107) lie outside the plot limits (at stdev = 4.0 − 5.5).

Figure 2

FASL frame it seems okay (for 112-FAFA there are not enough data to determine what is normal and what is exceptional).

- Images (other than BRFA or FAFA) that appear noisier in the figures above (0112, 0202) show a larger standard deviation; the mean does not seem to be affected (other images show a similarly elevated mean as the 0112 image, and the mean of 0202 agrees well with most of the smooth ones). It was found that this was due to a problem with `saltcombine` which was subsequently fixed and the noisiness disappeared.

- The average mean should be around zero but is ~ -0.6 for 2x2 frames and ~ -1 for 4x4 frames instead.

An investigation of the individual frames shows sometimes subtle patterns or wavelike structures which are usually smoothed out in the master frames, except when they are very pronounced (*e.g.*, on 0131, a bright/dark stripe pattern in extensions 1 and 2 of one image is still faintly visible in the

master image). Furthermore, often the left and right extensions of a CCD appear to be of different brightness, which seems to happen alternatively from one image to the next. In other words, when adding up the 'odd' and 'even' numbered frames into new master bias frames enhances the effect, see Fig. 3. This affects mainly the extensions 1 – 4 and is most obvious on the BRFA frames taken on 0107.

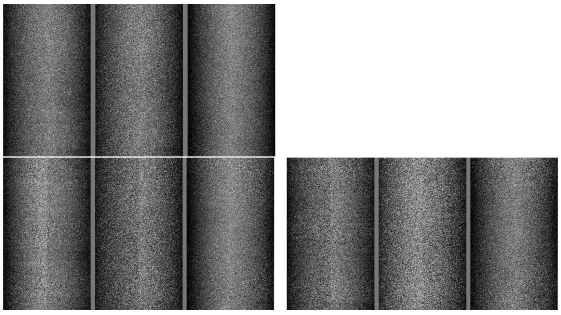

Figure 3: The master bias frame is at the top left; below are two 'sub-master' bias images made of 6 ('odd'; left) and the other 5 ('even'; right) images, respectively.

Conclusions:

- Bias frames other than with the faint/slow setting show distinct (and varying) patterns.
- Some bias frames how a gradient due to light leakage during twilight.
- Individual images can show structures (*e.g.*, stripes) or a variation in horizontal gradients which can also affect the bias frames.
- The mean counts of a frame are not zero but slightly negative (up to 1 count).
- A more detailed analysis of the individual images of the bias frames and the problems mentioned here can be found in the wiki report on RSS Bias analysis (Schröder, 2013a)[2].
- A simple analysis of mean counts reveals some variation of BIAS level in consecutive exposures. See report by Brent Miszalski (2011)[3].

Here are some recommendations for obtaining bias frames:

- Use only faint/slow settings.
- To avoid a gradient in the individual images caused by light leakage the dome shutter should be closed when taking bias frames during twilight.
- The first image in a series of bias frames taken appears often a bit noisier or shows structure and it may be better to observe 12 images and discard the first (or only combine images after visual inspection of them).

[2]https://sciencewiki.salt.ac.za/index.php/A._Schroeder_RSS_Bias_analysis
[3]http://wiki.salt.ac.za/index.php/File:MiszalskiBiasRep.pdf

3 Dark current level (Task #2)

Task: To determine dark current levels and analyze their relevance.

Data: Six exposures were taken in imaging mode with varying exposure time and filter. The characteristics are:

> 20130914, P041 – P046: imaging mode, filter PI06530, 600s (P041), 1200s (P042), 1800s (P046); filter PI08175 with 3600s (P043), 1800s (P044),and 1200s (P045); 2x2 binning, faint/fast.

Conclusions: Dark current level is non-existent at 0.0005 electrons/second.

4 Read noise and gain (Tasks #3 and #4)

Task: To test read noise and RSS detector gain.

Data: Any bias frames.

Analysis: For comparison, see the reports by Bologna & Carter (2009) on RSS testing in the lab and by Bologna (2011) on gain analysis.

Conclusions:

- Read noise is currently regularly monitored and updated at the telescope. Typically values are around 2.8 electrons for faint/slow mode, 3.8 electrons for bright/slow mode, 4.4 electrons for faint/fast mode, and 10 electrons for bright/fast mode.
- Gains are now working as reported in the lab after correcting the settings for the bright mode.
- Gains are currently regularly monitored. Typically values are around 1.7 ADU/electron for faint/slow mode, 3.7 ADU/electron for bright/slow mode, 3.0 ADU/electron for faint/fast mode, and 10 ADU/electron for bright/fast mode.

5 Acquisition of targets (Task #5, #6 and #7)

Task: To acquire single/mulitple targets and verify accuracy.

Data: Various.

Conclusions:

- Targets can be acquired. Initial pointings have an accuracy of 13". Offsets have an accuracy of 0.3".
- For an example of the analysis, see the report by Pickering (2011) on pointing analysis[4].
- For the LS, blind offsetting is not available. For faint sources, the use of an alignment star is suggested.

[4] http://wiki.salt.ac.za/index.php/20110303_pointing_analysis

- For the MOS:
  - The accuracy of ~ 0.3" can be routinely done if the PI-supplied reference stars have accurate astrometry.
  - The largest current challenge is the rotational drift of the pointing. This limits the use of narrow slits and the length of continuous exposures. A realignment might be necessary during a track.
  - See section 7.4.4 in the "Call for Proposals" for details and recommendations concerning MOS observations.

6 Stability of LS mask insertion (Task #9)

Task: To test the stability of wavelength calibration while moving the long slit in and out of the focal plane.

Data: Twenty exposures of the CuAr lamp were obtained with the tracker centered: The first ten exposures were taken repeatedly without any changes inbetween, while for the next ten exposures the slitmask was removed and re-inserted before each exposure. The characteristics are:

> 20130914, P047 – P066: 0.6" slit, PG3000 (gr-angle = 43.623, ar-angle = 87.265), filter PC00000, 240s, 2x2 binning, faint/slow.

Data reduction: I have used `specidentify` to overlay the arclamp calibration template CuAr.txt, fitted the data and dumped the x and lambda information of the identified features with 'p' to a file.

Analysis: The automated spectral identification task does not always identify the same lines in all images, and some lines were rejected as having too large residuals. A total of 32 lines were identified, equally distributed over the spectrum (from 4237.22 Å to 4889.04 Å). The number of identified lines per image varied from 22 to 27, and the standard deviation of the residuals after a successful fit varied between 0.025 and 0.039.

As reference image I chose P049 which had 27 lines out of the 32 automatically identified (there were a few others with the same number of lines but I preferred to use an image as close to the start of the series as possible). For the comparison, I measured the missing 5 lines by hand. I then calculated the difference in x for each image pair and for each identified line.

Figure 4 shows the mean of all lines per image (black dots). For the first ten images (left of the dotted line) there is no obvious trend with time, as expected (note that the trend seen in the RSS wavelength stability analysis is due to the motion of the telescope, while here the telescope was not moved). Once the slitmask was moved before an exposure, the mean positions of the lines become less stable: while for the next three exposures the mean position still seems to be at or close to the previous means, there seems to be a 'jump' after that and the mean positions of the lines on the final seven images again seem reasonably constant with time though the scatter between the means is larger than before.

Contrary to that, the scatter in the relative positions of the lines per exposure is the same for all exposures (red dots).

No variation between CCDs, wavelength or brightness of the lines could be found.

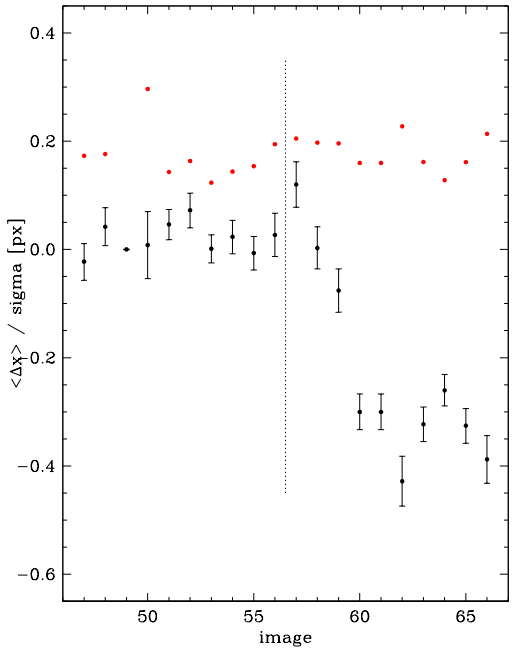

Figure 4: Mean difference in x position (black) and sigma (red) for all images.

Conclusions:

- The x-position of a line does not vary with time when the telescope is not moving.
  - The mean positional change of lines between exposures is 0.019 ± 0.010 pixel (or 0.0043 ± 0.0023 Ångström).
- Removing and re-inserting the slitmask causes the lines to move slightly with respect to the previous image.
  - The scatter in the mean positions is now 0.057 pixel / 0.0129 Ångström (taken for seven images) as opposed to 0.029 pixel / 0.0066 Ångström when the slitmask is not moved (10 exposures).
  - There happened a jump of $\sim$0.35 pixel / 0.0794 Ångström during the series of exposures where the slitmask was moved. It is not clear whether this was an exceptional jump (in a statistical sense), whether another jump would occur after a few more exposures, or whether it was due to some other singular (outside) influence.
- There is no noticeable dependence on wavelength or brightness of the line.

7 Stability of MOS mask insertion (Task #10)

Task: To test the stability of wavelength calibration while moving the MOS slit mask in and out of the focal plane.

Data: Ten exposures of the QTH lamp were obtained with the dome closed and the tracker parked: The mask was inserted and removed using the "Slitmask in" and "Slitmask out" buttons on PCON associated with the MOSCAL procedure. The slitmask was not stowed between observations but

was only removed from the beam. After each insertion, a 3-second image was observed. Further characteristics are:

20120229, P016 – P025: P000244N16 mask, filter PI05060, 3s, 2x2 binning, faint/slow.

Data reduction: All of the data were processed with `saltfirst` and centroids of the reference stars were automatically calculated using Sextractor. The centroids for each star across the ten images were compared and the mean position of each reference hole as well as the standard deviation calculated.

Analysis: Figure 5 displays the offset of each reference star from the mean in x and in y in each frame. The typical standard deviation in x was 0.015" and the typical deviation in y was 0.025". The deviations for each of the individual reference holes is shown in Table 2.

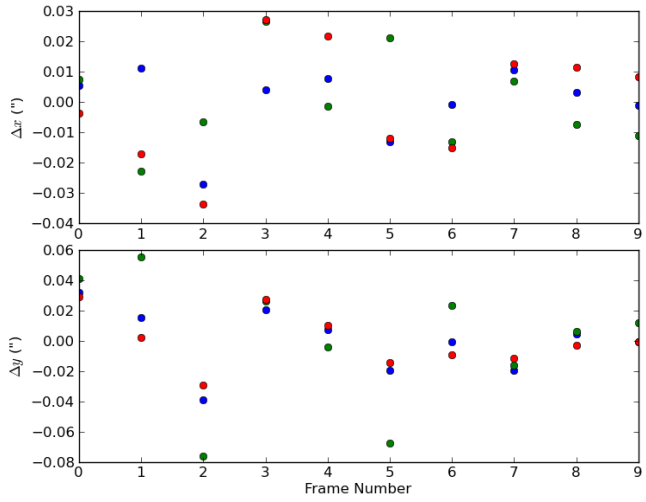

Figure 5: Offset of each reference star from the mean in x and in y versus frame.

Table 2: Deviations for each of the individual reference holes

x-position [px]	stdev ["]	y-position [px]	stdev ["]
894.69	0.015	577.11	0.017
1564.57	0.011	1036.94	0.041
2292.57	0.018	1763.82	0.020

Conclusions:

- Over small time scales an insertion has a stability of 0.014", 0.025" in x and y.
- Details of this analysis can be found in the wiki report by P. Väisänen (2012)[5].
- Further information can be found in the MOS report by P. Väisänen (2011)[6].
  - The repeatability of the mask position when re-inserting it multiple times at the same

[5]http://wiki.salt.ac.za/index.php/Stability_of_inserting_a_MOS_mask
[6]http://wiki.salt.ac.za/index.php/File:MOS_status_oct2011.pdf

Rho-angle and temperature etc. is very good, ∼0.05 unbinned pixels (< 0.01 arcsec) as calculated from a dataset from 20111011 files P90-P94.

– However, the accuracy is of the order of ∼2 unbinned pixels (∼0.25 arcsec) over different conditions, as calculated from 7 separate data sets and 80+ frames from late September to mid-October on a single mask. The field is obviously the same, but the track position changes slightly, with Rho within about 30 degrees or so over all the frames.

- These tests were taken with the old MOS mask holder. An investigation with the new mask holder is still outstanding at the time of this report.

8 Image quality (Task #11)

Task: To check on image quality, the PSF is measured as a function of focus and position on the image.

Data: Thirteen images with a series of focus settings 100 units apart were obtained. A mask with 12.5 micron pinholes in various positions across the FOV was used, see Fig. 6. The characteristics are:

20110419, P08-P20: P000000N03 (12.5μ pinholes), filter PC00000, 1.184s, 1x1 binning, faint/fast.

Data reduction: I have used the ds9 contours (at a contour level = 15 and smooth = 2) and regions to measure the position and size of each point. In some cases I have used an ellipse (*e.g.*, R5 in Fig. 7a) since the distribution of light across the defocused image of the point source was very uneven, but the major axis should be equivalent to the radius of the circles used in the other cases.

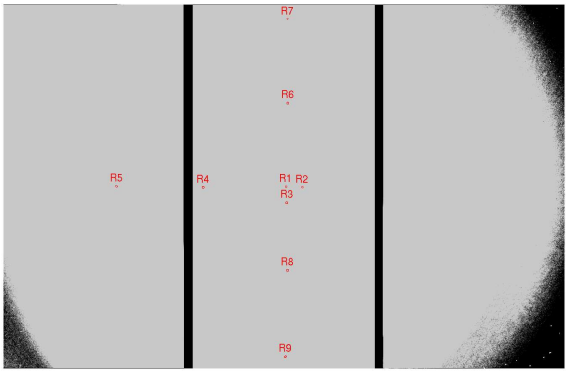

Figure 6: Image showing the distribution of points over the FOV and their numbering.

Analysis: Fig. 7a shows the variation of size and position with focus for each region except for R3 (which is similar to R1 and R2). For a more detailed analysis, Figs. 7b and 8 show the radius as well as the x and y position of each position as a function of focus setting.

Conclusions:

- Size:

  – The best focus seems to be around 650 – 800 with a preference for ∼700.

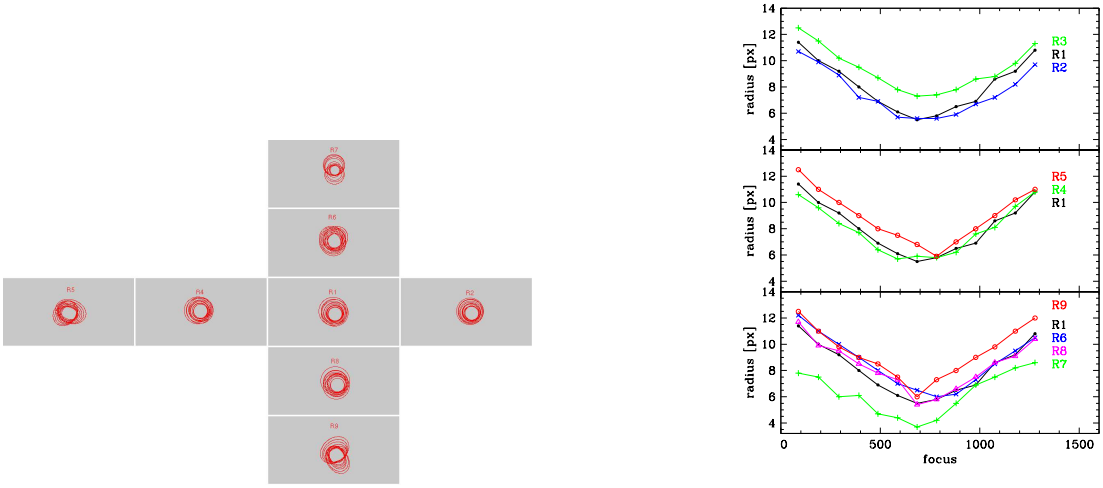

(a) The measured ds9 regions of each image are superimposed.

(b) Variation in radius with focus for the three central regions R1, R2 and R3 (top), the horizontally aligned regions R1, R4 and R5 (middle), and for the vertically aligned regions R7, R6, R1, R8 and R9 (bottom).

Figure 7

  - The minimum radius is around 5.5 pixel, the maximum around 12.5 pixel.
  - Per focus setting, there seems to be a variation of up to 2 pixels in radius across the FOV, with R3 and R9 being the largest, and R2 being the smallest (though there are no clear systematics).
  - R7 seems to have the smallest size by far for each setting but it is also the most distorted and faintest dot (possibly the 15-level contour is too faint for a good comparison).

- Position:

  - The position of the defocused image wanders slightly with focus setting (up to 2 pixels in x and up to 4.5 pixel in y). Note that the elliptical region does not represent the centre of the true (asymmetric) image very well, *cf.*, Fig. 7b.
  - Near the centre of the FOV (R1 – R3) the position of the defocused image of a point source wanders slightly both in x and y in the same direction for focus settings that are too small or too large (by 2 pixels at the most).
  - Towards the edge of the FOV the positional change with focus is not 'symmetric' around the best focus as for the central regions:
    * Points lying towards the left (R4, R5) keep wandering in x while the y-position changes symmetrically with focus (up to 3 pixels).
    * Points lying along the vertical axis (R9, R8, R6, R7) keep wandering in y (up to 5 pixels) while the x-position changes little or is nearly symmetrical around the best focus (up to 2 pixels).

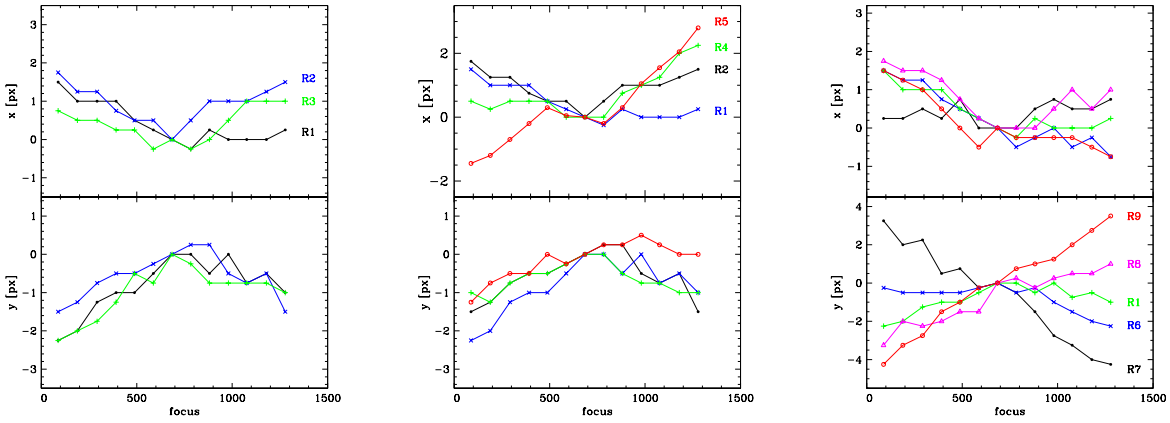

(a) Variation in positions x (top) and y (bottom) with focus for the three central regions R1, R2 and R3.

(b) Variation in positions x (top) and y (bottom) with focus for the four horizontally aligned regions R2, R1, R4 and R5.

(c) Variation in positions x (top) and y (bottom) with focus for the five vertically aligned regions R7, R6, R1, R8 and R9 (skipping R3).

Figure 8

– Towards the edge of the FOV the image of a point sources becomes more distorted with defocusing, and the position angle depends on whether the focus setting is too small or too large.

9 LS and MOS Image Quality and Focus Tasks (Tasks #12, #13, #17, #18)

Task: To verify the optimal focus as a function of position in the FOV.

Data: Eleven exposures were obtained with 'best' focus at 519 and with a series of focus settings 100 units apart. The same pinhole mask as for the 'Image Quality' task was used (*cf.*, Fig. 6), this time using the spectrograph. The characteristics are:

> 20130926, P34 – P44: P000000N03 (12.5μm pinholes), PG3000, (gr-angle = 43.62, ar-angle = 87.27), filter PC000000, 60.2s, 1x1 binning, faint/slow.

Data reduction: For each line I selected two regions per CCD plus the central position. Table 3 gives the x- and y-positions and the focus settings used. I used `imexam` to measure the centre of a line and the FWHM, and I averaged three measurements per position. The separation of the three lines in the middle test the resolution. As a consequence, the position and FWHM measurements for these lines were not always possible or meaningful (in particular, imexam could never measure line 2042 alone and line 2035 only sometimes).

Analysis: The *width* of the line (as a measure of focus) changes both with y-position and with x-position.

Table 3: Measurement parameters.

x-positions:	500, 1500, 2700, 3170, 3700, 5000, 6000
y-positions*:	124, 1100, 1860, 2022, 2035, 2042, 2984, 3934
focus positions:	100, 200, 300, 400, 500, 519, 600, 700, 800, 900, 1000

* These are only rough positions and change slightly from exposure to exposure

Figure 9a shows data for the line at y = 1860. The measurements at different x-positions are indicated by colour as explained in the legend. For the central chip (cyan, green and magenta) the best focus is in this case at 519. The focus for the 'red' (right-hand) chip (red and dashed black) is marginally better for focus 600, while the focus on the 'blue' (left-hand) chip gets progressively higher (600 for x = 1500 (blue) and 700 for x = 500 (black)). This same pattern (with slight variations) can be seen for all y-positions.

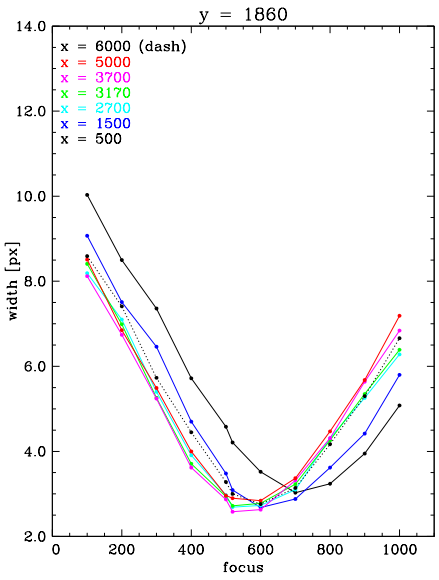

(a) The FWHM of the line at y = 1860 as a function of focus.

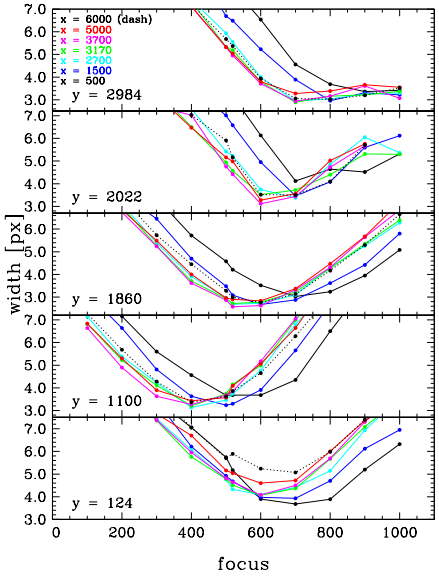

(b) The FWHM of the lines at y = 124, 1100, 1860, 2022, 2984 (bottom to top) as a function of focus.

Figure 9: FWHM of the lines as a function of focus.

Figure 9b shows the variation for all y-positions (y = 124, 1100, 1860, 2022, 2984 from bottom to top). Note that the measurements of line 2035/2042 were all affected by their merging and line 3934 was too faint/noisy for a good measurement. The focus setting with y-position seems to be lowest for line 1100, and highest for line 2984. Table 4 gives the deviation from the 'best' focus setting (as determined at the telescope) for each pair of x,y-coordinates (note that the 'best' focus was rounded down from 519 to 500 to make the numbers more readable!)

Conclusions:

- The best focus as measured by the FWHM of a line changes both with x- and y-position.

Table 4: Δ(focus setting) across the detector.

y-position	x = 500	x = 1500	x = 2700	x = 3170	x = 3700	x = 5000	x = 6000
2984	400	300	200	200	200	200	300
2022	200	200	200	100	100	100	200
1860	200	100	19	19	19	100	100
1100	100	0	-100	-100	-100	-100	-100
124	100	100	100	100	100	100	200

- The 'best' focus as determined at the telescope is best for a position on the central CCD but slightly below the middle.
- The largest deviation from the best focus on the detector (at a given focus setting) can be found in the top left corner.
  - In the upper half of the 'blue' (left-hand) CCD, the largest change in FWHM is about 4.5 pixel.
  - In the upper half of the 'red' (right-hand) CCD, the largest deviation in FWHM is about 2.5 pixel.
  - In the lower half of the (full) detector, the largest deviation in FWHM is about 1.5 pixel.

Further analysis regarding the change in y-position and resolution of the central lines can be found on the wiki page (Schröder 2013b)[7].

10 Guiding and Tracking (Task #15)

Task: To test the reliability of tracking, including reliability of open-loop rotation.

Data: The procedure here was to set the telescope tracking at a position and to configure BCAM to take an image every 30 – 60 seconds during the track. Dates with observations are: 20101204, 20101205, 20101206, 20101227, 20101228, 20110104, 20110105, 20110107, 20110110, 20110112, 20110115, 20110116, 20110207, 20110211, 20110213. This was done with the old system.

Data reduction: Drifts were analyzed in the XY image plane as well as for rho angles. Objects used to calculate the rho drift were located on the longslit at 4 arcminutes distance from the guide star (If the guide star is further away, the amplitude of the rho drift will be larger). The test duration was one hour.

Analysis: Figure 10 shows the drift on the sky ($\sqrt{\mathrm{RA}^2 + \mathrm{Dec}^2}$) and in rho angle. The red dots show the drift after the telescope's pointing model was updated. The linear drift has clearly improved with the new pointing model, while the rho drift seems about the same.

Conclusions:

- Old system: Assuming a good pointing model:
  - The average linear drift is about $0.5 - 0.8$ "/min;

[7] https://wiki.salt.ac.za/index.php/LS_focus_further_analysis

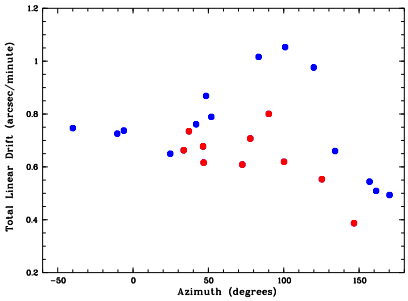

(a) Combination of the linear drift in RA and Dec in arcseconds per minute as a function of the azimuth of the telescope. Red dots show the drift after the pointing model update.

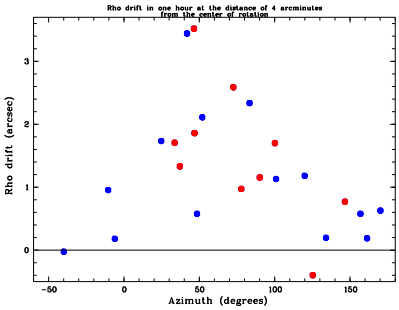

(b) Drift in rho angle of the telescope in arcseconds per minute as a function of the azimuth of the telescope. Red dots show the drift after the pointing model update.

Figure 10

  - The average rho angle drift is up to 0.015 deg/min.
  - While the linear drift can be corrected for by active guiding (using a single star), the rho drift will stay uncorrected during an observation.
  - Details of the analysis can be found in the report by Kniazev (2011)[8].

- New system:
  - There is no report for the new data, but they show the same pattern as for the old system, that is, the numbers and the azimuth dependence are reliable.

11 Distortion (Task #16)

Task: To measure the distortion and other aberrations.

Conclusions:

- The sky-to-detector transformation comes in two parts: the 'plate' transformation (that is, undistorted pixel positions) and the distortion of these positions.
- The transformation formulae and starting values can be found in Nordsieck 2012[9].

12 LS and MOS throughput (Tasks #19 and #20)

Task: To measure the system throughput.

Data: The latest result is from a burst-mode throughput measurement from 18th of March 2014:

20140318, P42 – P62: imaging mode, various filter, 30s, 2x2 binning, faint/fast.

[8]https://wiki.salt.ac.za/index.php/Old_Commissioning_Page#Open-Loop_Telescope_Tracking
[9]http://wiki.salt.ac.za/index.php/File:Coord-transform_120514.pdf

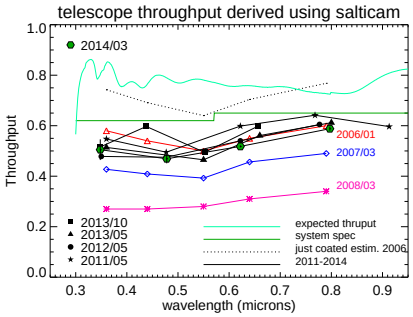

(a) Telescope throughput results from several years, the most recent determination is shown as the black curve through the green symbols. The expected throughput curve on top is close to the values included in the Simulator tools for Telescope optics.

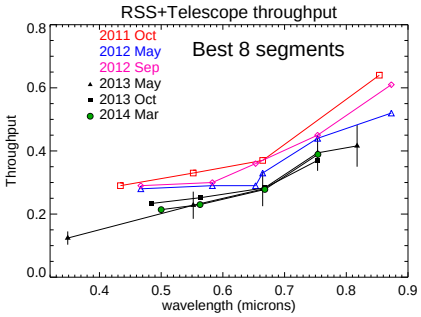

(b) Instrument + Telescope throughputs are shown as the blue and red symbols and curves, while the RSS-optics-only throughput is the black curve.

Figure 11

Data reduction: Electrons counted on the detector (arriving through the primary mirror, SAC, and all instrument optics) were determined as a function of wavelength. These are compared with the expected number for the given star. Filter transmission curves, individual detector quantum efficiencies, and extinction were taken out of the equation. All measurements were taken from the best 8 segments only.

Analysis: Since Salticam optics are simple, it has always been assumed that the Salticam measurement can be used to derive the "Telescope throughput". Thus dividing the Salticam throughput by the "known" Salticam optics and Fold Mirror efficiencies (*i.e.*, assuming that the FM and all anti-reflective coating losses on Salticam optics are nominal), results in the Telescope (Primary mirror + SAC) throughput. The latest results of such throughput is shown in Fig. 11a with the March 2014 determination as the black curve and green hexagons. Results from previous measurement campaigns are also shown as indicated.

The values are in the same 50% – 60% range as they have been since 2011 (*cf.*, the other black curves in the image) with perhaps marginal evidence for a slight decline since 2011. (The 2013 point at 4300Å is suspect). Note that the 2006 to 2008 throughput was obtained during the time when the primary mirror was not cleaned at all. But we are still short of where we should be.

The RSS + Telescope throughput is shown in Fig. 11b with the March 2014 results with a black curve through green points. There seems to be a decline from 2011, but it is difficult to disentangle from anything happening inside the SAC with this measurement. However, the 2014 points actually line up very well with all the 2013 values.

To arrive at the RSS-optics only throughput, the RSS + Telescope optics can be divided by the Telescope value from Fig. 11a. The computed values are given in Table 5. A plot showing the actual RSS only throughput from 2011 is shown in Väisänen & Kniazev (2011, their Fig. 1).

A final caveat: the burst mirror based absolute throughput measurements were based on the average of 8 brightest segments. If, instead, the average of brightest 40 segments on a fairly central track were used (which would reflect a realistic case of a science observation) the calculated telescope throughput would decrease by a factor of 1.25 in the bluest measured RSS filter, 1.20 in the other filters, and 1.18 in the reddest filter.

Table 5: RSS throughput values.

wavelength [Ångström]	percentage wrt 2013	comment
3600	35%	from 2013
5000	45%	
6500	54%	
7500 – 8000	68%	

Conclusions:

- Telescope throughput and RSS optics contribute similar amounts to the total system throughput. The total system throughput at the moment is significantly lower than expected, 0.2 in the blue to 0.4 in the red.
- The RSS optics system throughput (0.3, blue, to 0.7, red) is lower than the expected ~ 0.8 level.
- Tests in 2011 of the same sources observed "simultaneously" with RSS and SCAM showed RSS / SCAM count ratios of 0.5 – 0.6.
- This analysis is described in an e-mail from Väisänen 2014[10].
- Details of the 2011 analysis (together with a comparison with the simulator) are presented in Väisänen & Kniazev (2011).
- Further details on the 2012 and 2013 analyses were presented at the respective board meetings.

13 LS calibration (Task #23)

Task: To verify the change in spectrum shape with position across the FOV.

Data: Five exposures of the standard star LTT7987 placed at different y-positions were used. The characteristics are:

> 20130826, P02 – P06: PL0400N001 mask, PG0900, (gr-angle = 15.5, ar-angle = 31.0), filter PC03850, 60.2s, 2x2 binning, faint/slow.

Data reduction: I have reduced the spectra using `pysalt`. Instead of using arc lamp data I used `caltype=rss` in `specrectify`. I extracted the spectra using the following sections for P02 – P06, respectively: [194:220], [604:630], [988:1014], [1373:1399], [1752:1778].

Analysis: To visualize the change in spectrum shape, I divided each spectrum by the central one. Figure 12 shows the colour-coded result for all spectra: black is the central one (by definition a straight line), blue and red are at smaller y-position, while green and red are at higher y-positions.

The shape changes less than 10% in total, and mainly at the ends of the spectrum. The spectra

[10] https://wiki.salt.ac.za/index.php/LS_tput_analysis

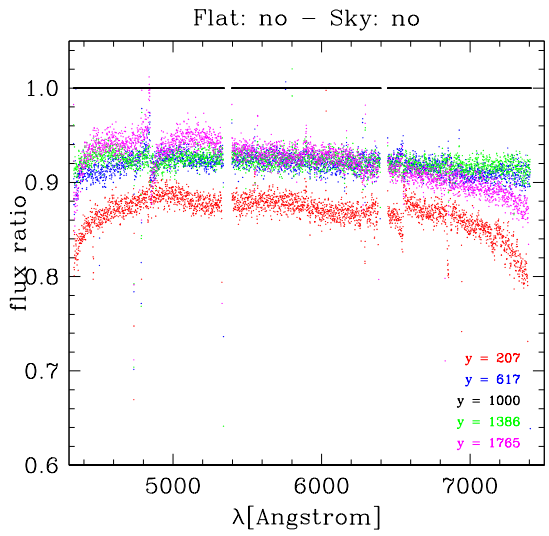

Figure 12: The ratios of the spectra at different y-position with respect to the central one; red at the bottom (y = 207 px); blue in the lower half (y = 617 px), green in the top half (y = 1386 px) and magenta at the top (y = 1765 px).

near the y-edges (red and magenta) show more extreme changes in the shape while the central ones (blue and green) are almost flat. The data have not been flat-fielded, so all spectra are fainter as compared to the central one. While the top-most spectrum (magenta) is equally bright to the two closer to the centre, the bottom-most (red) is clearly fainter and shows the most extreme change in shape.

For a clearer view, Fig. 13a shows pairs of spectra, while Fig. 13b shows individual spectra divided by each other (in particular interesting to show the change of shape between the bottom half and the top half of the detector).

- The two closest to the centre in the top panels (blue and green) are very similar with a maximum change of $\sim 2\%$ (wrt to the central one as well as wrt each other).
- The two spectra at the edges of the detector (red and magenta) show a different brightness to each other (since the spectra were not flat-fielded), and ignoring that difference in brightness, there is a slight slope of $\sim 4\%$ (Fig. 13b top middle panel; also ignored are the differences due to absorption line features, *e.g.*, at ~ 4000Å).
- The two spectra near the edges show the largest change in shape with respect to the central spectrum, in particular at the ends of the spectra (*i.e.*, extreme x-positions):
  - The spectrum at the bottom (red) shows that largest deviations with $\sim 6\%$ at the blue end and $\sim 8\%$ at the red end, while the middle part (~ 4600Å – ~ 6800Å is reasonably straight with deviations of up to $\sim 2\%$);
  - The spectrum at the top (magenta) shows deviations of $\sim 6\%$ at the blue end, and $\sim 7\%$ at the red end. There is a more pronounced slope across the whole spectrum compared to the lowest spectrum (*cf.*, Fig. 13b, top middle panel).

Conclusions:

- The change of shape of a spectrum away from the central line is $< 10\%$.

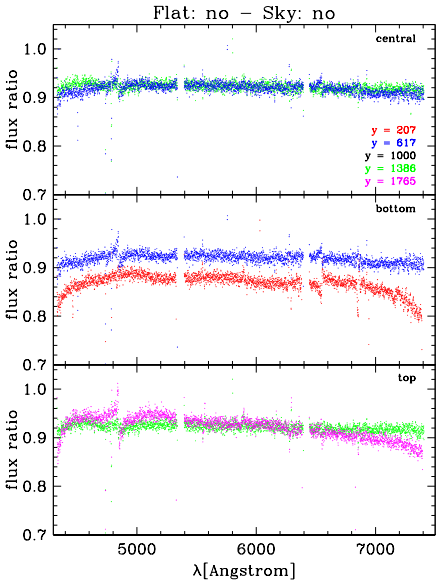

(a) Pairs of the ratios of spectra with the central one are shown. Top panel: the two middle spectra; middle panel: the two top spectra; bottom panel: the two bottom spectra.

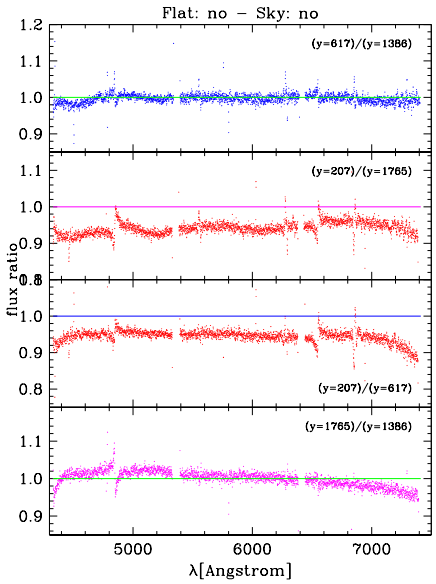

(b) Individual ratios of spectra are shown. Top panel: the two central spectra divided by each other; top middle panel: change of shape in spectra near the top and bottom edge; bottom middle panel: change of shape in spectra in the bottom half of the detector; bottom panel: change of shape in spectra in the top half of the detector.

Figure 13: FWHM of the lines as a function of focus.

- The most extreme deviations occur at the ends of the spectra (*i.e.*, extreme x-positions).
  - Across the inner 90% of the spectrum (x-position) the maximum deviation is $\sim 5\%$.
- The deviations are more pronounced near the bottom and top edges of the detector (y-position).
  - The change of shape of a spectrum placed in about the inner 2/3 of the detector (y-position) is $< 3\%$.
- Spectra in the top half of the detector show a slight slope with x-position which is more pronounced the further to the top the spectrum is placed.

14 LS UV performance (Task #24)

Task: To verify the UV performance on real data and comparing it to the simulator.

Data: Three standard star observations were used.

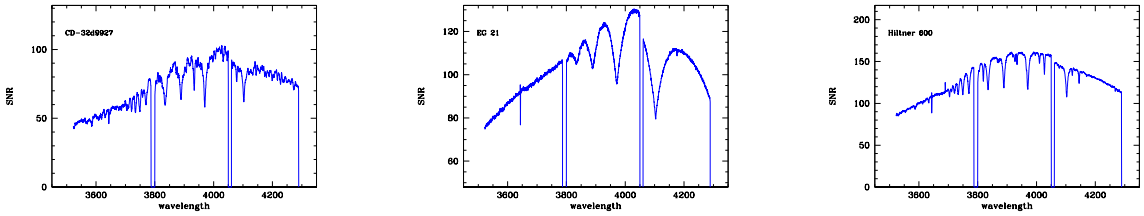

(a) Observed SNR for star CD-32d9927.

(b) Observed SNR for star EG 21.

(c) Observed SNR for star Hilton 600.

(d) Simulated SNR for star CD-32d9927.

(e) Simulated SNR for star EG 21.

(f) Simulated SNR for star Hilton 600.

Figure 14

CD-32d9927: P20130820 with P08, 60sec
EG21: P20130826 with P88, 60sec
HILT600: P20131009 with P37, 120sec
The other characteristics are:

PL0400N001 mask, PG3000, (gr-angle = 34.0, ar-angle = 72.25), filter PC00000, 2x2 binning, faint/slow.

Data reduction: I have reduced the spectra using `pysalt`. Instead of using arc lamp data I used `caltype=rss` for `specrectify`. I extracted the spectra using the following sections:
CD-32d9927: [978:1008]
EG21: [990:1019]
HILT600: [1046:1075]

Analysis: The output of `specextract` gives a list with wavelength, flux and error (Poissonian). To get the signal-to-noise ratio (SNR) I divided the flux by the error. These are shown in Fig. 14 top row.

I then used the simulator with the input spectra downloaded from the ESO site, using settings according to the specifics of each observations (effective area, seeing, zenith distance). For spatial resolution the SNR was calculated per resolution point, for spectral resolution it was calculated per bin. The results are shown in Fig. 14 bottom row.

The results are not conclusive: while CD-32d9927 and Hilton 600 have a too high simulated SNR,

the SNR for EG21 is too low. There were clouds reported for CD-32d9927 and partly cloudy for Hilton 600 which could explain the difference. However, if EG 21 was indeed unaffected by clouds, the simulator seems to underestimate the SNR. On the other hand, the shape of the two SNR curves of EG21 are qualitatively more different than the shapes of the curves of the other two stars and a comparison here is more doubtful. Table 6 summarizes the results.

Table 6: Observing conditions and SNR measurements for each exposure.

St.star	AM	effective area	estimated seeing	photometric conditions	SNR UV end [sim/obs]	SNR maximum [sim/obs]	SNR red end [sim/obs]
CD-32d9927	1.29	427800	1.3”	cloudy	70	130	90
					50	100	80
EG21	1.24	400200	4”	clear	70	80	55
					80	130	95
Hilton 600	1.25	404800	1”	partly	160	220	135
				cloudy	90	160	120

Conclusions:

- The signal-to-noise ratios of standard stars observed in the UV differ between observations and the simulator.
- The reasons for this difference are likely non-photometric conditions, and it would be best to repeat the test under photometric conditions.

15 MOS UV performance (Task #25)

Task: To verify the UV performance on real data and comparing it to the simulator.

Data: Two MOS observations of the south galactic pole region were used. The characteristics are:

> 20130902, P37 and P38: P001083N03 mask, PG0900 (gr-angle = 12.875, ar-angle = 25.75), PC03200, 664s, 2x2 binning, faint/slow.

Data reduction: I have reduced the spectra using `pysalt` using the ThAr arc lamp observation P39. I extracted the spectra using the sections listed in Table 7. Among the observed objects were two galaxies (one was observed with a tilted slit and is not useable) and two quasars.

Analysis: The output of `specextract` gives a list with wavelength, flux and error (Poissonian) per exposure. I calculated the mean of the two exposures and to get the signal-to-noise ratio (SNR) I divided the flux by the error. These are shown in Fig. 15 top row.

I then used the simulator with the exposure-specific input (including zenith distance 32°, effective area 427800, seeing $1\farcs4$) for a longslit set-up (since the y-dependence of the MOS is not yet implemented). The individual choices on the spectra are listed in Table 8 together with the SNR values. For spatial resolution the SNR was calculated per resolution point, for spectral resolution it was calculated per bin. The objects are treated as point sources. The results are shown in Fig. 15

Table 7: Extraction regions for each exposure.

Slit ID	Extraction region P37	Sky region	Extraction region P38	Sky region
GAL2	[14:39]	[9:16]	[18:34]	[8:15]
QSO1	[21:32]	[10:16]	[22:33]	[12:19]
QSO2	[21:33]	[9:15]	[21:33]	[9:17]

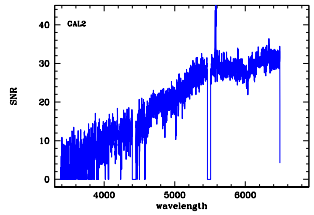

(a) Observed SNR for GAL2.

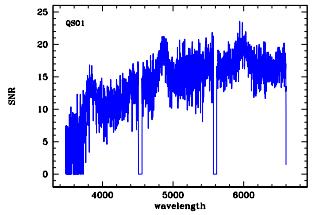

(b) Observed SNR for QSO1.

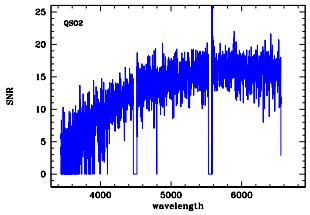

(c) Observed SNR for QSO2.

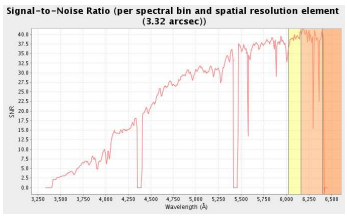

(d) Simulated SNR for GAL2.

(e) Simulated SNR for QSO1.

(f) Simulated SNR for QSO2.

Figure 15

bottom row. The SNR calculations are very good. Note that if the galaxy were assumed as being extended in the simulator, the agreement with the real data is not as good (this is mainly because the galaxy is very small and barely extended on the image).

Conclusions:

- The signal-to-noise ratios of faint and point-like objects observed in the UV show a reasonable agreement between observations and the simulator.

16 Imaging ADC verification (Task #26)

Task: Primary verification of performance of atmospheric dispersion corrector.

Data: No data obtained yet.

Table 8: Spectrum settings in the simulator and SNR measurements for each object.

Object	spectrum	R-band	redshift	SNR UV end [sim/obs]	SNR maximum [sim/obs]
GAL2	E-gal	$17\overset{\text{m}}{.}6$	0.02	3	40
				5	32
OSO1	power law	$19\overset{\text{m}}{.}2$	2.09	5	15
	$\alpha = -1.5$			6	17
QSO2	power law	$19\overset{\text{m}}{.}8$	0.87	3	10
	$\alpha = -1.5$			4	16

Conclusions:

- This task will be done at a later stage at medium priority.

17 LS ADC verification (Task #27)

Task: Verify performance of atmospheric dispersion corrector with slit.

Data: Two sets of observations were taken: (i) Sixteen exposures of the standard star 1709324 while tracking; (ii) five exposures each on two nights of Tyc 9154-1124-1 with widely different TRKRHO settings. The characteristics are:

(i) 20111024, P01 – P15: no mask ID, PG0900 (gr-angle = 12.875, ar-angle = 25.76), filter PC00000, 10.2s (except P01 which is 5.2s), 2x2 binning, faint/slow (except P01 which is faint/fast). Time between exposures are about four minutes. The rho angle (TRKRHO) changes from −1.82 to −1.92. The total sequence spans about 50 minutes

(ii) 20111220, P12, P14, P16, P18, P19: PL0400N001, PG0900 ([gr-angle,ar-angle] = [12.5,25.0] for the first two exposures and [18.5,37.0] for the other three exposures), filter PC00000, 60.2s (except P18 which has 1.2s), 2x2 binning, faint/slow, TRKRHO $\simeq -0.17, -0.09, 1.45$. The total sequence spans about 20 minutes.

20120106, P259, P260, P262, P263, P265: PL0400N001, PG0900 ([gr-angle,ar-angle] = [12.5,25.0] for the first four exposures and [18.5,37.0] for the last exposures), filter PC00000, 10.2s (except P259 which has 60.2s), 2x2 binning, bright/slow (except P259 which is faint/fast), TRKRHO $\simeq -0.16, 1.4$. The total sequence spans about 15 minutes.

Table 9 gives the airmass, rho-angle and grating settings for each exposure.

Data reduction: I used `imexam` to measure the centre of a line and the FWHM, and I averaged three measurements per position. I selected 11 positions in x (three per CCD plus edges): x = 10, 500, 1180, 1900, 2600, 3170, 3800, 4400, 5100, 5800, 6315.

Analysis: The point of interest of this task is to see how the shape (*i.e.*, y-position as a function of x) of the spectrum changes while tracking (*i.e.*, as a function of rho angle). I have analyzed

Table 9: Observing parameters. Airmass in brackets is an estimate.

	20111024:									
Extension	P01	P02	P03	P04	P05	P06	P07	P08	P09	P10
TRKRHO	−1.822	−1.825	−1.831	−1.837	−1.846	−1.855	−1.864	−1.882	−1.891	
Airmass	(1.197)	(1.214)	1.223	1.238	1.252	1.267	1.282	1.299	1.316	
gr-angle	12.875	12.875	12.875	12.875	12.875	12.875	12.875	12.875	12.875	12.875
ar-angle	25.75	25.75	25.75	25.75	25.75	25.75	25.75	25.75	25.75	25.75
Extension	P11	P12	P13	P14	P15					
TRKRHO	−1.900	−1.909	−1.919	−1.923	−1.925					
Airmass	1.333	(1.342)	1.374	1.384	1.387					
gr-angle	12.875	12.875	12.875	12.875	12.875					
ar-angle	25.75	25.75	25.75	25.75	25.75					
	20111220:					*20120106:*				
Extension	P12	P14	P16	P18	P19	P259	P260	P262	P263	P265
TRKRHO	−0.170	1.430	1.463	−0.094	−0.096	−0.152	−0.164	1.415	1.413	1.395
Airmass	(1.252)	(1.252)	1.252	1.253	1.253	(1.244)	1.245	1.247	1.247	1.248
gr-angle	12.5	12.5	18.5	18.5	18.5	12.4975	12.4975	12.4975	12.4975	18.5
ar-angle	25.0	25.0	37.0	37.0	37.0	25.0	25.0	25.0	25.0	37.0

P20111024, with the continuous change of rho angle while tracking, separately from P20111220 and P20120106, each of which compares two widely different rho angle settings.

(i) 20111024:

Figure 16a shows the difference of the y-position with respect to the measurements of the second image P02 (note that the first image had a different readout speed) for all rho angles (in the order of "black – blue – cyan – green – magenta – red" and "solid line – dotted line – dashed line"). While the first exposure (P01, solid black line) shows a considerable offset, the others seem to slowly change the shape.

As can be seen, the absolute y-position drifts with time, and so I subtracted the mean Delta(y) for each exposure. Figure 16b shows the shifted lines in groups of similar shapes (and consecutively in time!).

Finally, to quantify the change in shape I have calculated the mean and the standard deviation of the Delta(y) over all x for each exposure and show this in Fig. 16c. The standard deviation increases with time from ≤ 0.1 px between adjacent exposures to ~ 0.4 px at the end of the observing run (that is, about 50 minutes later).

(ii) 20111220 and 20120106:

As above, Fig. 16a shows the difference of the y-position with respect to the measurements of the first image for P20111220 (top panel) and with respect to the second image for P20120106 (bottom panel) for the five rho angles.

To correct for the drift between the exposures, I subtracted the mean Delta(y) for each exposure. Figure 16b shows the shifted lines in groups of similar shapes (and consecutively in time!). It seems that the shape is similar for similar rho angles for a given observing run (but differs with date). Note the small number of points, though.

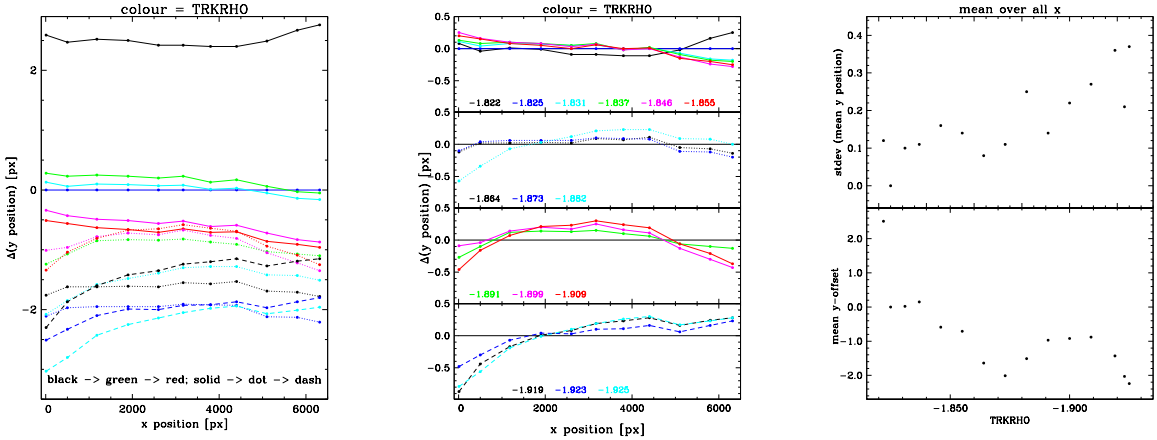

(a) The difference in y-position with respect to P02 is shown for all exposures.

(b) The shifted differential y-positions grouped by exposures/rho angle as indicated in each panel.

(c) The standard deviation and the mean of the Delta(y) positions plotted versus rho angle.

Figure 16

As for P20111024 I have calculated the mean and the standard deviation of the Delta(y) over all x for each exposure and show this in Fig. 16c. For better comparison I show the groups of negative and positive rho angles in separate windows (left and right panels, respectively). The standard deviation increases slightly from 0.7 px for negative rho angles to 1.0 px for positive rho angles. Also the mean seems to be dependent on rho angle, changing from −2.9 px for negative rho angles to −16.6 px for positive rho angles. There is also a possible dependence on observing run (or setting, that is, GAINSET faint vs bright). However, there are not enough points to be sure.

Conclusions:

- The shape (in y) of a spectrum line changes slowly while tracking:
  - The maximum relative deviation in y is +0.3 px and −0.9 px after about 50 minutes (where the deviation after 15 minutes is already ±0.03 px);
  - The standard deviation from the mean (*i.e.*, flat) Delta(y)-position increases with time (on average by ∼0.3 px over 50 minutes);
- The shape (in y) of a spectrum line changes with rho angle:
  - The maximum relative deviation in y is −4 px and +2 px when changing from TRKRHO = −0.17 to 1.4;
  - The standard deviation from the mean (*i.e.*, flat) Delta(y)-position increases by up to 2 px when changing from TRKRHO = −0.17 to 1.4;
- The absolute y-position drifts while tracking:
  - After 50 minutes the y-position has drifted by ∼2 px;

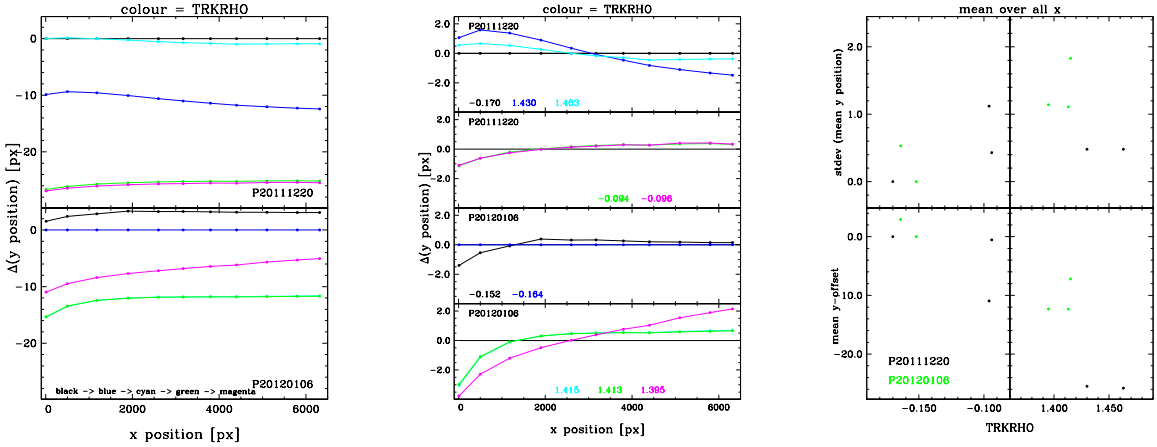

(a) The difference in y-position with respect to the first image for P20111220 (top) and with respect to the first image for P20111220 (bottom).

(b) The shifted differential y-positions grouped by exposures/rho angle as indicated in each panel.

(c) The standard deviation and the mean of the Delta(y) positions plotted versus rho angle.

Figure 17

  - The drift in y is not linear but moves back and forth;

- The absolute y-position changes with rho angle:
  - The y-position drifted between 6 px and 25 px when changing from TRKRHO = −0.17 to 1.4;
  - The drift possibly depends on the setting of GAINSET and ROSPEED;

18 LS flat-fields (Task #28)

Task: Test efficacy of flat-fielding.

Conclusions:

- Many PIs use calibration screen flat fields for spectroscopic data frames in case of faint and/or extended targets.
- Beyond approximately 8000 Ångström there is significant fringing present on the frames (*cf.*, Sec. 21), and flats taken together with the science frames are essential for all target types in this case.
- In addition, for both sky and fringing removal for fainter and/or extended targets in these reddest settings it is also helpful to dither along the slit between the (two or more) science frames. The dither step must be larger than the extent of the target.
- A full report by Alexei is in progress.

19 Imaging flat-fields (Task #31)

Task: Test efficacy of flat-fielding.

Data: Various.

Conclusions:

- Twilight/calibration flats show variation over the field of view with Rho and other telescope parameters.
- The central region can be flatted with twilight flats taken at the same Rho as the data.
- For best results, flats should be created from the data itself by dithering between each observation.
- A detailed report of SALTICAM and RSS flat-fielding was done by Mohan 2011[11].
- Tracking while taking twilight flat-fields reduces the residuals to $\sim 0.1\%$, see Ted Williams e-mail[12].
- For the effect of fringing see Sec. 20 below.

20 Imaging Fringing (Task #121)

Task: Investigation of fringing on RSS imaging flat-fields with particular emphasis on the fringing at red wavelengths.

Data: Various flat-fields of RSS Imaging between 20110101 and 20111206 with filters settings 'PI08%' and 'PI07%' were used.

Data reduction: The frames were spilt into groups according to filter and lamp. Each group was made into a normalized master flat using the median `flatcombine` function in IRAF, and divided by the median of the combined frame. The median of the combined frame is taken from the central illuminated portion, [540:1040,100:900] and [1080:2080:200:1800] for 4x4 and 2x2 binning, respectively.

Analysis: Four rows and four columns were selected as representative slices across the master flat, evenly distributed across the frame. A sixth order polynomial was fit to each row and column slice and the percent variation ('peak-to-through' variation) from the fit is calculated and plotted.

Conclusions:

- Fringing is significantly more obvious for arcs than for QTH lamps. Peak-to-through percent variations are
  - $\sim 2\%$ for Sky and QTH lamps for all filters (*i.e.*, no fringing is apparent in these frames);
  - $\sim 5\%$ for arcs and PI07390 and PI07535;

[11] https://sciencewiki.salt.ac.za/index.php/File:Vm_flat_report.pdf
[12] https://wiki.salt.ac.za/index.php/RSS_flatfield_analysis

  - $\sim$15 – 20% for arcs and PI08350 and PI08730;
  - $\sim$10% for arcs and PI08535.

- Fringing increases with filter wavelength, but more data are needed to characterize a pattern.
- For t eh full report including details on t eh data and plots of the variations along t eh slices can be found in Gulbis 2011[13].
- Future work includes determining the wavelength limit for which the effect becomes substantial.

21 LS Fringing (Task #122)

Task: Investigation of fringing on RSS spectroscopic frames.

Data: Three data sets with QTH2 flat-fields were used:

(i) Extended source IRAS 19254-7245 for the detailed investigation: 20120809, P01 – P09; 900s for the target and 5s for each flat-field;

(ii) Bright point source HD 184492 to check fringe removal in case of short exposures and bright targets: 20120929, P28 – P37; 4s for the target and 8s for each flat-field;

(iii) A series of QTH2 flats with a range of exposure times and ND filter settings to check how the fringe pattern scales with the level of counts on t eh detector: 20130522, P01 – P12; 0.2 – 10 seconds.

The other characteristics are:

PL0100N002 mask, PG1300 (gr-angle=33.5, ar-angle=67.0), filter PC04600, 2x2 binning, faint/slow.

Data reduction: Cuts were plotted along the target spectrum and along sky lines after different versions of t eh reduction process (for details see Väisänen 2013[14]).

Analysis: There is significant fringing on the thinned back-lit detectors of RSS frames red-ward or 7500 Ångström. A good correction can be done using calibration screen flat-fields taken together with the dataset, but for the best fringe (and sky) removal multiple frames with offsets along the slit, dithering, is required. The latter would be necessary for diffuse and faint sources while flats only are needed for bright objects.

Conclusions:

- Fringes can be removed from RSS spectroscopic data.
- The best approach is to use calibration flats to divide out the majority of fringing. Any residual component can be removed by subtracting a combined 2D frame constructed from dithered science frames.

[13] http://wiki.salt.ac.za/index.php/File:SALT.2254AA0001.v2.1.pdf
[14] http://wiki.salt.ac.za/index.php/File:SALT_RSS_fringing.pdf

- Recommended method:
  - For fainter, diffuse targets use the full method
  - For bright objects which are well over the sky background level, the division by flat-fields appears to be sufficient.
- The details of the fringing analysis and the methods on removal can be found in Väisänen 2013[15].

22 LS and MOS wavelength verification (Tasks #32 and #33)

Task: To verify the wavelength range and chip gaps as predicted by the simulator.

Data: The same data as for LS_uv and MOS_uv were used:

(i) One LS-exposure of the standard star CD-32d9927 with the wavelength coverage 3500Å – 4300Å:

20130820, P08: PL0400N001 mask, PG3000, (gr-angle = 34.0, ar-angle = 72.25), filter PC00000, 60sec 2x2 binning, faint/slow.

(ii) One MOS-exposure of the South Galactic Pole region with the wavelength coverage 3400Å – 6500Å:

20130902, P37: P001083N03 mask, PG0900 (gr-angle = 12.875, ar-angle = 25.75), PC03200, 664s, 2x2 binning, faint/slow.

Data reduction: I have reduced the spectra using `pysalt`. Instead of using arc lamp data I used `caltype=rss` for `specrectify`. I extracted the spectra using the following sections:

(i) 20130820, P08: [978:1008]

(ii) 20130902, P37: [14:39]

Analysis: I compared the wavelength limits at the edges of each CCD with the RSS simulator using the exposure-specific input. The results are shown in Table 10. While for the high-resolution grating the differences are about 10 Ångström or less, the deviations for the low-resolution grating are around 50 Ångström.

Conclusions:

- For the LS PG3000 grating the difference in wavelengths between observation and simulator is $< 1.7\%$ (with respect to the wavelength range of 770Å).
- For the MOS PG0900 grating (y-offset = 900 px) the difference in wavelengths between observation and simulator is $< 3\%$ (with respect to the wavelength range of 3100Å).

[15] http://wiki.salt.ac.za/index.php/File:SALT_RSS_fringing.pdf

Table 10: Wavelength comparison.

Instrument	Date and Exposure	Detector start	Gap-1 start	Gap-1 end	Gap-2 start	Gap-2 end	Detector end
LS	20130820, P08	3523	3786	3800	4049	4061	4289
	simulator	3522	3777	3801	4036	4062	4279
	difference	1	9	−1	13	−1	10
MOS	P20130902, P37	3373	4400	4451	5463	5507	6489
	simulator	3407	4329	4408	5408	5486	6394
	difference	−34	71	43	55	21	95

23 LS resolution (Task # 35)

Task: To test on-sky resolution.

Data: One observation of V2487 Oph with many sky lines was used:

> 20120530, P83: PL0150N001 slit mask, PG0900 (gr-angle = 20.375, ar-angle = 40.75), PC04600, 957s, 2x2 binning, faint/slow.

Data reduction: I have used `imexam` to measure 29 isolated sky lines at the centre of the detector (y = 1025 pixel), that is, taking the mean of three single FWHM measurements.

Analysis: Figure 18 shows the FWHM in Ångström as a function of x-position. The CCD gaps are indicated by vertical lines. Except for the bluest lines, the FWHM is fairly constant across the detector, though the scatter seems to decrease with wavelength. This may be partly due to the varying focus across the detector (*cf.*, Sec. 9), but the bluest sky lines are also fainter on average than the red sky lines.

The mean FWHM is 6.0 pixel or 5.6 Ångström. The median is the same.

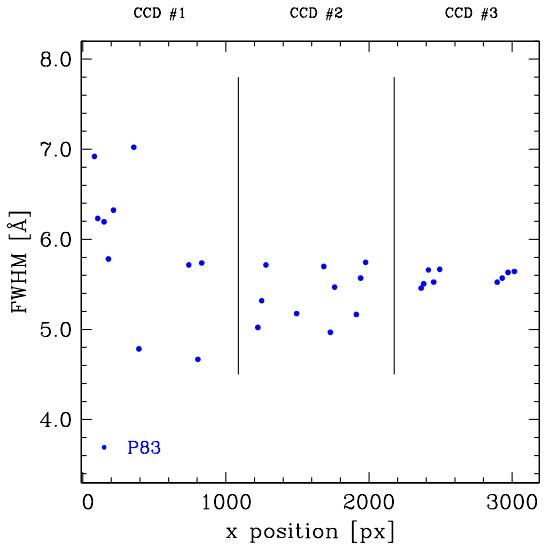

Figure 18: FWHM in Ångström of sky lines as a function of x-position.

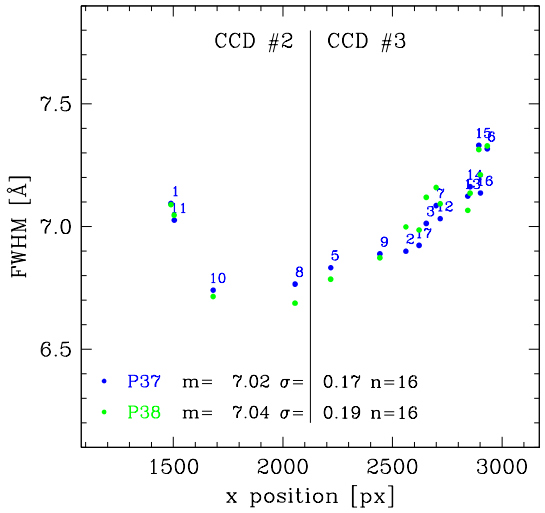

Figure 19: FWHM in Ångström of the bluest sky line as a function of x-position.

Conclusions:

- The mean FWHM is 5.6 Ångström.
- The bluest lines have a larger FWHM but also show a larger scatter between lines.
- The FWHM is practically the same as what the simulator predicts, that is, 5.5 Ångström.

24 MOS resolution (Task #36)

Task: To test on-sky resolution.

Data: The same data as for MOS_uv were used, that is, two exposures of the South Galactic Pole region:

> 20130902, P37: P001083N03 mask, PG0900 (gr-angle = 12.875, ar-angle = 25.75), PC03200, 664s, 2x2 binning, faint/slow.

Data reduction: I have used `imexam` to measure the FWHM of the bluest (single) sky line in each spectrum (in case where this line fell onto a chip gap I used a fainter line which had comparable FWHM in case where both lines were visible).

Analysis: Figure 19 shows the FWHM in Ångström as a function of x-position (that means also, as a function of slit position) for both images P37 and P38. The gap between CCDs 2 and 3 is indicated. There are no lines on CCD 1. Except for the two lines at ∼1500 px (extensions 1 and 11) the FWHM changes monotonously with x-position. The mean FWHM is 7.0 Å (or 7.2 px), while the simulator gives for this setting a FWHM of 7.7 Å.

Conclusions:

- The mean FWHM is 7.0 Ångström.

- The FWHM is larger for slit positions away from the centre of the detector.
- The FWHM repeats well over two subsequent observations.
- The FWHM is marginally smaller than what the simulator predicts, which is 7.7 Ångström.

25 LS Stray Light Tests (Task #38)

Task: To determine level of stray light and looking for features.

Data: Observations with two grating angles were taken for a series of exposure times (60s, 180s, 300s, 600s) and with with the cal screen in and out (and with the dome closed). The characteristics are:

20131210 with P55 - P62 ('blue'): 1.5" slit (PL0150N001), PG0900 (gr-angle = 12.125, ar-angle = 24.25), filter PC00000, 2x2 binning, faint/fast.

20131210 with P63 - P70 ('red'): 1.5" slit (PL0150N001), PG0900 (gr-angle = 20.0, ar-angle = 40.0), filter PC00000, 2x2 binning, faint/fast.

Data reduction: Visual inspection of the images and using `imstat` to get the statistics per CDD. I used `imexam` with a 9x9 pixel box and measured the bright line as well as the faint line at three y positions (centre and ∼300 pixels from the edges; each three times) and the background around it (once to the left and once to the right).

Analysis:

Blue: Visually nothing can be seen (except a 'shadow' of the 1. gap), see Fig. 20a. Table 11 gives the means per CCD.

Table 11: Statistics for LS-blue.

Exposure	Exp-time	Cal screen	Median [el/ksec/CCD] CCD#1 / #2 / #3
P55	60s	in	1.1 / −3.1 / −0.5
P56	180s	in	2.6 / 1.2 / 2.1
P57	300s	in	3.0 / 2.7 / 2.3
P58	600s	in	3.2 / 3.4 / 2.8
P59	60s	out	1.1 / −4.2 / −0.9
P60	180s	out	2.9 / 1.8 / 2.0
P61	300s	out	3.1 / 2.6 / 2.7
P62	600s	out	3.3 / 3.3 / 2.8

Red: Visually one bright line on CCD 1 is visible (left), while on CCD 3 (right) a faint line appears when the cal screen is out, see see Fig. 20b. Nothing visible with cal screen in (except for the 'shadow' of the 1. gap also seen in the blue). I present the mean values in Table 12.

There is significant light in the bright line when the cal screen is out, at about 7-sigma (this

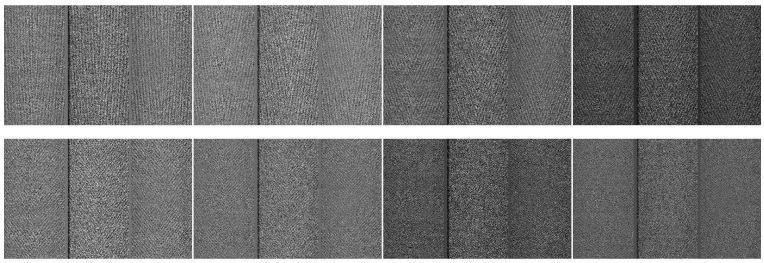

(a) Ds9 tile of LS-blue observations, with the exposure time increasing from left to right; top row with cal screen in, bottom row with cal screen out.

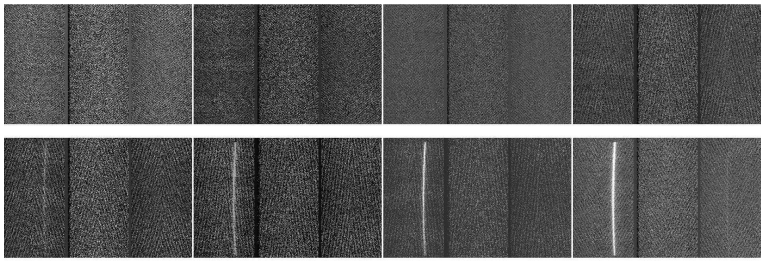

(b) Ds9 tile of LS-red observations, with the exposure time increasing from left to right; top row with cal screen in, bottom row with cal screen out.

Figure 20

could be a 0.order spectrum or reflection off the collimator). The diffuse areas are enhanced by about a factor 2. With cal screen in there is no additional light. The statistics per CCD are barely affected by the additional light.

Conclusions:

- With cal screen out, bright lines may appear on the image, depending on the grating.
  - They are significantly brighter than the background (about 7 times).
  - They disappear fully when the calscreen is in.
- With cal screen out, faint and diffuse lines may appear on the image, depending on the grating.
  - They are only about $2-2.5$ times brighter than the background.
  - They seem to disappear fully when the calscreen is in (but *cf.*, the straylight for the MOS where this is not the case).

26 MOS Stray Light Tests (Task #39)

Task: To determine level of stray light and looking for features.

Data: Observations with two grating angles were taken for a series of exposure times (60s, 180s, 300s, 600s) and with with the cal screen in and out (and with the dome closed). The characteristics are:

20131017 with P12 - P19 ('blue'): P001083N03 mask, PG0900 (gr-angle = 12.125, ar-angle = 24.25), filter PC00000, 2x2 binning, faint/fast.

Table 12: Statistics for LS-red.

Exposure	Exp-time	Cal screen	Median [el/ksec/CCD] CCD#1 / #2 / #3	Mean bright strip (bgd) [el/ksec]	Mean diffuse strip (bgd) [el/ksec]
P63	60s	in	1.3 / −2.5 / 0.6	5.9 (10.3)	4.6 (8.2)
P64	180s	in	2.8 / 2.4 / 2.9	2.9 (4.2)	4.3 (4.8)
P65	300s	in	3.0 / 2.9 / 3.4	2.9 (4.2)	4.3 (4.8)
P66	600s	in	3.3 / 3.5 / 3.8	3.9 (3.5)	4.2 (4.3)
P67	60s	out	2.9 / 0.7 / 1.4	45 (10.4)	13.6 (14.4)
P68	180s	out	4.6 / 2.2 / 3.3	43 (5.9)	7.6 (4.9)
P69	300s	out	4.7 / 3.2 / 3.8	43 (6.0)	8.3 (3.8)
P70	600s	out	4.6 / 3.6 / 4.1	44 (7.4)	8.5 (5.1)

20131017 with P20 - P27 ('red'): P001083N03 mask, PG0900 (gr-angle = 20.0, ar-angle = 40.0), filter PC00000, 2x2 binning, faint/fast.

Data reduction: Visual inspection of the images and using `imstat` to get the statistics per CDD and `imexam` with a 9x9 pixel box to measure the features: the bright spots were measured each three times with the background around it (once above and once below). For the diffuse areas I used six measurements, taking the background above and below.

Analysis:

Blue: Visually, some bright spots appear on CCD 3 (right) when the cal screen is out but not when it is in, see Fig. 21a. Nothing visible with cal screen in. Table 13 shows the statistical results.

Table 13: Statistics for MOS-blue.

Exposure	Exp-time	Cal screen	Median [el/ksec/CCD] CCD#1 / #2 / #3	Mean bright spots (bgd) [el/ksec]
P16	60s	in	2.0 / 1.0 / -0.3	0.5 (-0.4)
P17	180s	in	3.9 / 3.3 / 2.3	2.5 (2.8)
P18	300s	in	4.2 / 4.0 / 3.0	2.8 (3.4)
P19	600s	in	4.4 / 4.4 / 3.3	3.2 (3.0)
P12	60s	out	2.2 / −1.6 / 0.2	109 (1.8)
P13	180s	out	4.0 / 3.6 / 3.1	114 (5.9)
P14	300s	out	4.4 / 4.5 / 3.6	116 (5.7)
P15	600s	out	4.6 / 4.8 / 3.7	114 (5.5)

Red: Visually, several bright dots appear on CCD 1 (left), while on CCD 3 (right) some faint and diffuse areas appear when the cal screen is out, see Fig. 21b. Nothing visible with cal screen in. The mean values are given in Table 14.

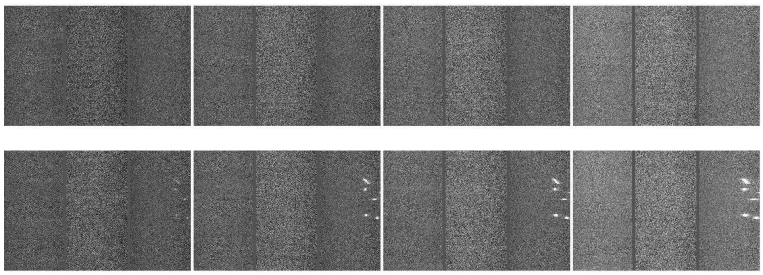

(a) Ds9 tile of MOS-blue observations, with the exposure time increasing from left to right; top row with cal screen in, bottom row with cal screen out.

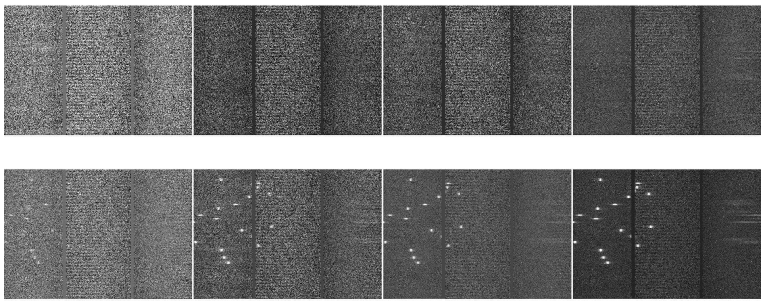

(b) Ds9 tile of MOS-red observations, with the exposure time increasing from left to right; top row with cal screen in, bottom row with cal screen out.

Figure 21

Conclusions:

- With cal screen out, bright lines may appear on the image, depending on the grating.
  - They are significantly brighter than the background (about 16 times).
  - They disappear fully when the calscreen is in.
- With cal screen out, faint and diffuse lines may appear on the image, depending on the grating.
  - They are only about $2 - 2.5$ times brighter than the background.
  - They may not disappear fully when the calscreen is in (they are about 1.5 times brighter than the background).

27 FP Stray Light Tests (Task #40)

Task: To determine level of stray light and looking for features.

Data: Observations without grating were taken for a series of exposure times (60s, 180s, 300s, 600s) and with the cal screen in or out (and with the dome and louvres closed). The characteristics are:

20140117 with P17 - P24: P000000N00 mask, PG0900 (but articulation = 0, gr-angle = 0), filter PC00000, 2x2 binning, faint/fast.

Table 14: Statistics for MOS-red.

Exposure	Exp-time	Cal screen	Median [el/ksec/CCD] CCD#1 / #2 / #3	Mean bright spots (bgd) [el/ksec]	Mean diffuse stripes (bgd) [el/ksec]
P20	60s	in	1.8 / 3.4 / 0.4	5.0 (5.5)	6.0 (1.7)
P21	180s	in	3.6 / 4.0 / 3.4	3.9 (3.9)	6.7 (4.3)
P22	300s	in	3.9 / 3.7 / 3.8	4.3 (4.1)	6.7 (4.9)
P23	600s	in	4.2 / 4.3 / 4.1	4.4 (4.3)	6.8 (4.2)
P24	60s	out	2.5 / 3.0 / 0.5	101 (5.0)	13 (5.3)
P25	180s	out	3.9 / 3.5 / 3.8	101 (6.0)	12 (3.9)
P26	300s	out	4.4 / 3.8 / 4.1	103 (6.4)	12 (4.5)
P27	600s	out	4.6 / 4.4 / 4.3	102 (6.7)	12 (4.6)

Data reduction: Visual inspection of the images and using `imstat` with a 9x9 pixel box to sample the brightest area in the centre as well as the fainter area near the edge of the FOV (at top, bottom, left and right) 6 times. These are compared to the area just outside the FOV (also top, bottom, left and right).

Analysis: The image of the FOV looks smooth and vignetted in both cases (cal screen in and out),

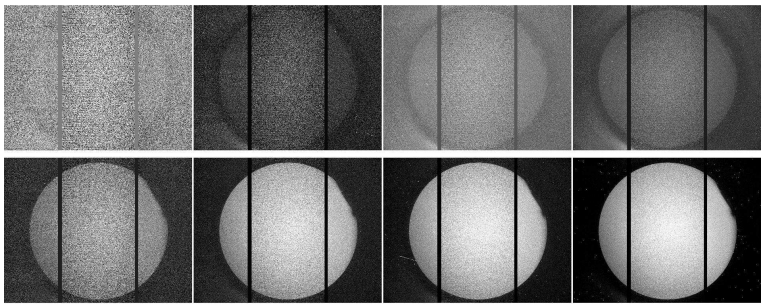

Figure 22: Ds9 tile of FP observations, with the exposure time increasing from left to right; top row with cal screen in, bottom row with cal screen out.

see Fig. 22. With the cal screen out the FOV is much brighter than the surrounding area, though. The mean statistical values for the centre, the edges and outside the FOV are presented in Table 15.

Note that the brightest part of the FOV is slightly offset between cal screen in ((x:y) $\simeq$ (1570:1010)) and cal screen out ((x:y) $\simeq$ (1650:1040)). For better comparison I have taken the mean of these two spots (the differences per image can be up to 5%).

There is significantly more light coming into the FOV when the cal screen is out (about 5 – 6 times), while the area outside the FOV is only slightly enhanced (about a factor of 2).

Conclusions:

- With cal screen out, the ambient light inside the FOV is enhanced by about a factor of 6, while outside the FOV it is enhanced by about a factor of 2.
- The centre of the vignetting function shifts slightly between cal screen in and cal screen out.
  - The brightness between these two spots can vary up to 6%.

Table 15: Statistics for Fabry Perot.

Exposure	Exp-time	Cal screen	Mean centre [el/ksec]	Mean edges of FOV [el/ksec]	Mean outside FOV [el/ksec]
P21	60s	in	48	31	15
P22	180s	in	41	27	17
P23	300s	in	42	27	16
P24	600s	in	42	28	17
P17	60s	out	224	156	32
P18	180s	out	232	150	36
P19	300s	out	230	152	30
P20	600s	out	230	154	31

28 Imaging Stray Light Tests (Task #41)

Task: To determine level of stray light and looking for features.

Data: Observations without grating were taken for a series of exposure times (60s, 180s, 300s, 600s) and with the cal screen in or out (and with the dome and louvres closed). The characteristics are:

> 0140117 with P09 - P16: P000000N00 mask, PG0900 (but articulation = 0, gr-angle = 0), filter PC00000, 2x2 binning, faint/fast.

Data reduction: Visual inspection of the images and using `imstat` to get the statistics per CDD and of the visible features. I used `imexam` with a 9x9 pixel box to sample the brightest area in the centre as well as the fainter area near the edge of the FOV (at top, bottom, left and right) 6 times. These are compared to the area just outside the FOV (also top, bottom, left and right).

Analysis: The image of the FOV looks mostly smooth and vignetted in both cases (cal screen in and out) though in case of the cal screen out the FOV is much brighter than the surrounding area, see Fig. 23b. In addition, in case of the cal screen out a faint ring-like feature appears in the lower part with a diffuse brighter spot to the left, see Fig.imgstray1plotb (bottom row). The mean statistical values are presented in Table 16.

I have also checked the faint features by taking 6 measurements of the bright spot to the left, comparing it with the surrounding region, and of the darker ring, comparing it to the brighter area just below in a region just right to the centre line (about (x:y) = (1807:436) and (1817:415), respectively).

Note that the brightest part of the FOV is slightly offset between cal screen in ((x:y) $\simeq$ (1500:890)) and cal screen out ((x:y) $\simeq$ (1610:1095)). For better comparison I have taken the mean of these two spots (the difference per image is between 3% and 6%).

There is significantly more light coming into the FOV when the cal screen is out (about 6 times), while the area outside the FOV is only slightly enhanced (less than a factor of 2). The bight spot is about 6% brighter than the surrounding area, while the ring-like feature is very faint, there is only about 2% difference between the darker and the brighter part (note that the measurements of the same area with cal screen in varies also up to 2% but this is due to the general lower count rate and the variation is not consistent across the exposures). All variations are independent on exposure time.

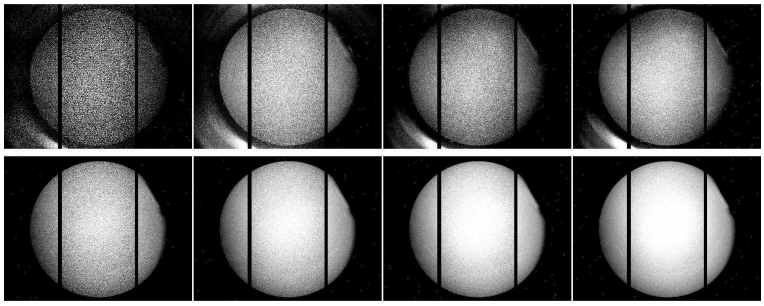

(a) Ds9 tile of Imaging observations, with the exposure time increasing from left to right; top row with cal screen in, bottom row with cal screen out.

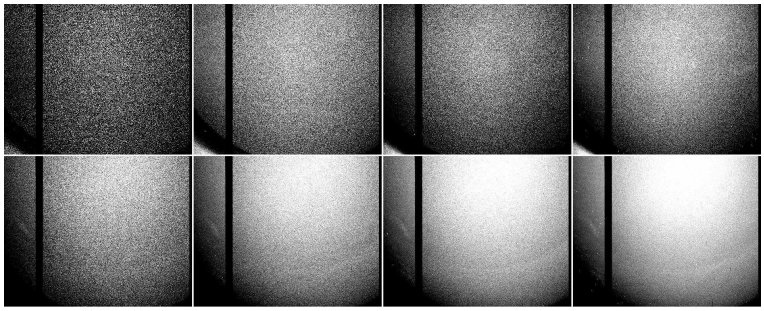

(b) Zoomed-in ds9 tile of Imaging observations, with the exposure time increasing from left to right; top row with cal screen in, bottom row with cal screen out.

Figure 23

Conclusions:

- With cal screen out, the ambient light inside the FOV is enhanced by about a factor of 6, while outside the FOV it is enhanced by about a factor of 2.
- The centre of the vignetting function shifts slightly between cal screen in and cal screen out.
  - The brightness between these two spots can vary up to 6%.
- Some faint structure can appear with cal screen out.
  - These features show a $2-6\%$ change in brightness.

29 Timing accuracy (Task #123)

Task: To test the absolute and relative timing accuracy of RSS slotmode data.

Data: A series of experiments were carried out by placing an LED in the payload light path, and an independent GPS was used to trigger it.

(i) 20120911, P11 – P30: slotmode (mask 144), PI06645 filter, 0.08 – 0.1s, GPS pulses of width 1μs or 10μs spaced at either 0.5s or 1s, 9x9, bright/fast.

(ii) 20121108P01 – P78: PC00000 filter, 0.08s, 9x9, bright/fast. The LED was triggered multiple times throughout the dataset, at varying pulse frequencies.

Table 16: Statistics for Imaging.

Exposure	Exp-time	Cal screen	Mean centre [el/ksec]	Mean edges of FOV [el/ksec]	Mean outside FOV [el/ksec]	Ratio 'bright spot:bbg'	Ratio 'darker ring: brighter ring'
P09	60s	in	305	208	101	0.98	0.99
P10	180s	in	300	210	103	1.01	1.00
P11	300s	in	301	210	98	1.00	1.02
P12	600s	in	300	212	101	1.01	1.01
P13	60s	out	1865	1325	185	1.07	0.98
P14	180s	out	1867	1328	184	1.06	0.99
P15	300s	out	1865	1324	186	1.06	0.98
P16	600s	out	1870	1325	186	1.05	0.98

Data reduction: The data were reduced through the standard SALT pipeline. To determine the signal, the mean ADUs for each slotmode frame (across all amplifiers) were calculated. Times were read from the headers, which represent the time at the start of each frame.

Analysis: The initial results indicate that the relative timing was good to within measurable accuracy (half an exposure time, which was on the order of hundredths of a second) and that the absolute timing was late by seven exposure times. SALTICAM data showed the same effect, because the header times were in fact the *readout* times rather than the exposure times – this timing offset was corrected in the pipeline. Additional tests, of data cubes containing multiple sequences of varying-cadence GPS pulses, demonstrate that the relative accuracy is good to within a few milliseconds and the absolute accuracy is not constant over time and can be off by up to 16 milliseconds.

Conclusions:

- The relative accuracy is good to within a few milliseconds.
- The absolute accuracy is not constant over time and can be off by up to 16 millisecond.
- The full analysis can be found in Gulbis 2013[16].

30 LS Point Spread Function (Task #43)

Task: To measure stellar PSF, including extended low-level pedestal.

Data: The brightest standard star observation (HILT600) from the task LS_uv was used. The characteristics are:

> 20131009, P37: PL0400N001 mask, PG3000, (gr-angle = 34.0, ar-angle = 72.25), filter PC00000, 120s, 2x2 binning, faint/slow.

Data reduction: I selected 7 positions in x for a profile measurement: x = 210, 625, 1370, 1585,

[16] http://wiki.salt.ac.za/index.php/File:SALT.2129AA001.pdf

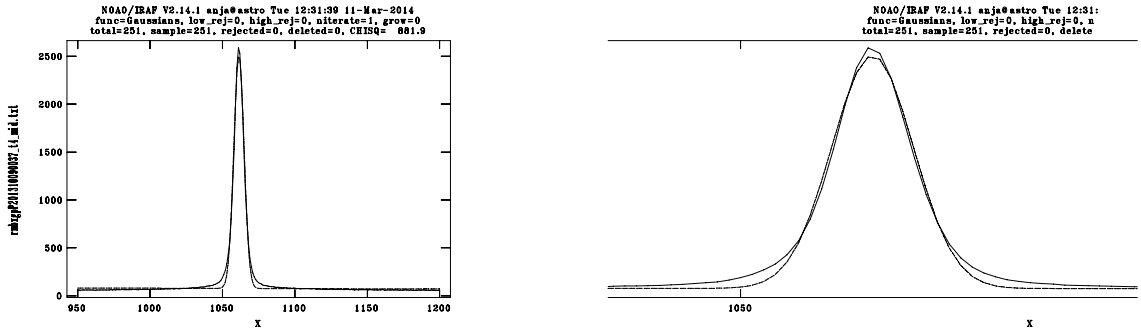

(a) Line profile at x = 1585 px (solid line) with the Gaussian fit shown as dashed line.

(b) Zoom in.

Figure 24

1940, 2500, 2970 pixel, with Delta x = 80 pixels (the uneven distribution comes from avoiding cosmic rays near or on the spectrum).

Analysis: I plotted the mean counts along the y-axis for each x-position and fitted a Gaussian using the IRAF task `ngaussfit` in `stsdas -> analysis -> fitting`. Figure 24 shows the example of the line at x = 1585 px: Fig. 24a shows the full fit from y = 950 – 1200 px, and Fig. 24b shows a zoom in of the profile: the solid line is the data, the dashed line the fit. The fitted Gaussian has a slightly lower peak and is narrower at the base. Table 17 gives the details of all seven profiles.

Table 17: Gaussian profile fits.

x-position [px]	mean [px]	FWHM [px]
210	1060.506	8.625
625	1060.736	8.478
1370	1061.219	8.350
1585	1061.383	8.333
1940	1061.658	8.434
2500	1062.134	8.411
2970	1062.648	8.351

Conclusions:

- The FWHM of a Gaussian fit to the line profile is about 8.3 – 8.4.
  - The FWHM is largest at the blue end (small x-positions).
  - The profile is not a pure Gaussian, instead it has faint wings (not further characterized).
- The centre of the line shifts slightly by ∼2 pixel across the width of the detector.

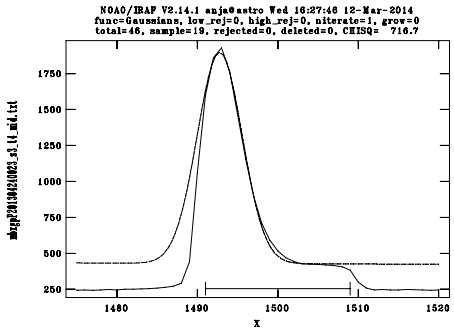

(a) Line profile at x = 1585 and y = 1493 (solid line) with the Gaussian fit shown as dashed line. The range used for the fit is indicated at the bottom.

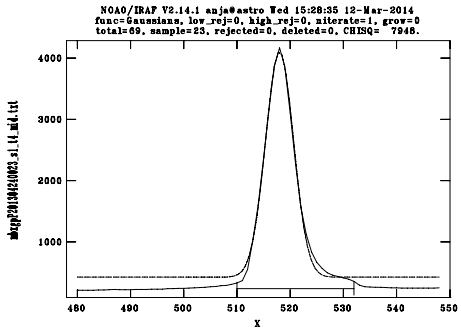

(b) Line profile at x = 1585 and y = 518 (solid line) with the Gaussian fit shown as dashed line. The range used for the fit is indicated at the bottom.

Figure 25

31 MOS Point Spread Function (Task #44)

Task: To measure the stellar PSF, including the extended low-level pedestal.

Data: I used bright star observations from a star cluster:

> 20130424, P23: P000778N01 mask, PG3000 (gr-angle = 39.9 ar-angle = 79.8), filter PC00000, 850s, 2x2 binning, faint/slow.

Data reduction: As for LS_psf, I selected 7 positions in x for a profile measurement: x = 200, 750, 1370, 1585, 1850, 2500, 3000 pixel, with Delta x = 80 pixels (the uneven distribution comes from avoiding cosmic rays near or on the spectrum).

Table 18: FWHM from Gaussian profile fits.

y-position [px]	x=200 px	x=750 px	x=1350 px	x=1585 px	x=1850 px	x=2500 px	x=3000 px
1660	7.75	7.55	6.79	7.32	7.07	7.19	7.21
1493	6.72	6.47	6.31	6.59	6.45	6.17	5.82
1023	6.34	6.23	6.02	5.91	5.90	5.84	5.76
518	6.88	6.55	6.26	6.18	6.04	6.10	5.90

Analysis: I plotted the mean counts along the y-axis for each x-position and fitted a Gaussian using the IRAF task `ngaussfit` in `stsdas -> analysis -> fitting`. Table 18 gives the FWHM of all four spectra (id'd by their y-position) at the seven x-positions. Note that the PSF measurements for the MOS are less accurate than for the LS due to the small length of the slit which means there is not much baseline next to the spectrum. In some cases the line was cut off by the lower end of the slit and the width of the Gaussian is thus less certain. Figure 25a shows as an example the spectrum at y = 1493 px and at x = 1585 px: The estimated slit region is indicated by the bar below the line: it is obvious that the line is asymmetric (as compared to the fitted (dashed) line), and the sky level

is the base to the right of the line. In case of spectra near the bottom of the detector, the line is more centered, but in such cases the sky level is more difficult to estimate, see as an example the spectrum at y = 518 px and at x = 1585 px shown in Fig. 25b.

Conclusions:

- The FWHM of a Gaussian fit to the line profile using the MOS varies from 5.8 to 7.8.
  - The fit is uncertain due to the short length of the slits
  - The FWHM is smallest to the right (in the 'red') and largest towards the top of the detector (large y).

32 LS stability (Task #59)

Task: To measure repeatability of an observation with the same instrument configuration over time.

Data: Three different data sets were used, all using the CuAr lamp and exposures were taken continuously until the track ended.

(i) 20130502, P097 – P110: PL0150N001 mask, PG3000 (gr-angle = 43.625, ar-angle = 87.265), filter PC00000, 180s, 2x2 binning, faint/slow. The time interval between two exposures was always the same, that is, about 197 seconds

(ii) 20131210, P01 – P33: PL0200N001 mask, PG2300, (gr-angle = 32.0, ar-angle = 64.0), filter PC00000, 100s, 2x2 binning, faint/slow.

(iii) 20131210, P36 – P54: PL0100N002 mask, PG2300, (gr-angle = 32.0, ar-angle = 64.0), filter PC00000, 200s, 2x2 binning, faint/slow.

Data reduction: I have used `specidentify` to overlay the arclamp calibration template CuAr.txt, fitted the data and dumped the x and lambda information of the identified features with 'p' to a file.

Analysis: The automated spectral identification task does not always identify the same lines in all images, and some lines were rejected as having too large residuals. For the analysis, the exposure with the largest number of identified lines was used as reference.

(i) A total of 32 lines were identified over all exposures, equally distributed over the spectrum (from 4237.22Åto 4889.04Å). The number of identified lines per image varied from 25 to 31, and the standard deviation of the residuals after a successful fit varied between 0.026 and 0.039.

Since P100 had all but one line out of the 32 automatically identified, I used it as a reference (and added the missing line by hand). I then calculated the difference in x for each image pair and for each identified line and plotted the mean deviation of all lines per image versus image number (in black, with error bars) and show the sigma in red in the same plot, see Fig. 26a.

There is a clear trend of the mean deviation with time, while the sigma shows only a marginal trend, and the scatter of the points is much smaller than the variation in Delta(x) with time.

I have looked for other dependences and found that the blue lines (on CCD1) drift faster than

the red lines (on CCD3) as shown in Fig. 26b. The sigma is now constant with time, and the slight increase in scatter noticed in Fig. 26a can be explained by the fanning out of the the Delta(x) of the lines with increasing distance to the reference image.

Note that the number of lines used for calculating the mean and sigma is small, that is, at maximum 13, 11, and 8 lines per CCD 1, 2, and 3, respectively. The same trend could be discerned on each CCD as well, that is, the trend is a function of position across all CCDs and not a function of CCD number.

As a last check, I selected the 7 brightest and seven faintest lines, making sure that they are similarly distributed over the x position (to avoid recovering the effect described above). Figure 26c shows the result: there is no trend visible.

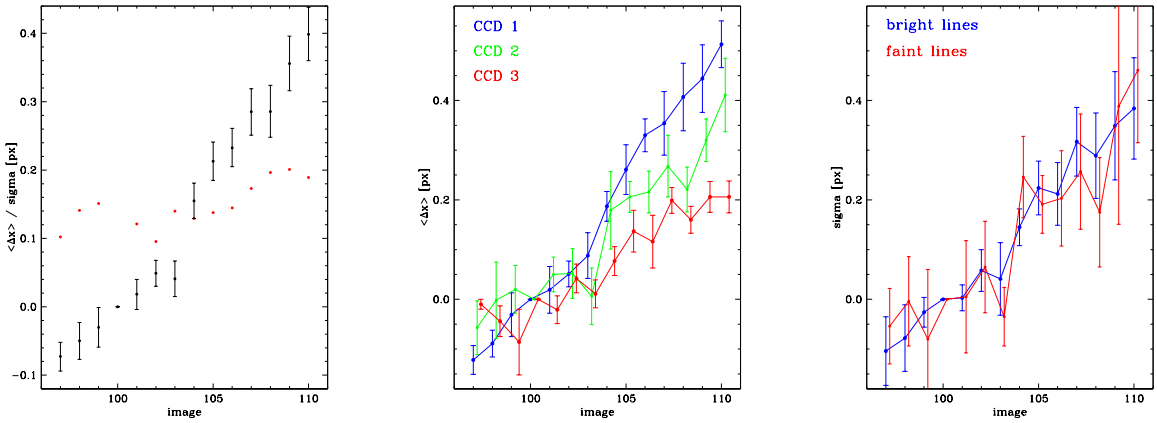

(a) Mean deviation in x position (black) and sigma (red) for all images.

(b) Mean deviation in x position of the lines grouped by CCD (as counted from left to right). For clarity, the points are slightly offset to each other in image number.

(c) Mean deviation in x position of the bright lines (black) and faint lines (red). For clarity, the points are slightly offset to each other in image number.

Figure 26

(ii) Between 21 and 30 lines were identified. Exposure P16 was taken as reference frame with 30 lines identified, and the standard deviation of the residuals after a successful fit varied between 0.14 and 0.27.

As above, the mean x-position of the lines varies with time (though here in the other direction), see Fig. 27a. The rate is 0.249 px/hr or 0.165 Å/hr

To investigate the stability of the solution of the transformation from pixel to wavelength, I first verified that the drift rate is independent on the method, that is, applying the solution of exposure P16 to all measured x-positions gave a rate of 0.162 Å/hr. Next, Fig. 28a shows the drift of the first parameter in the solution (a_0 in a third order Legendre polynomial) with time. The rates is 0.067 Å/hr.

The latter is smaller as the ones calculated above, which is due to the fact that all the parameter in the Legendre polynomial change from one solution to the next. To illustrate this, Fig. 28c shows the difference in calculated wavelength (with respect to the first image) for the solutions of three different images.

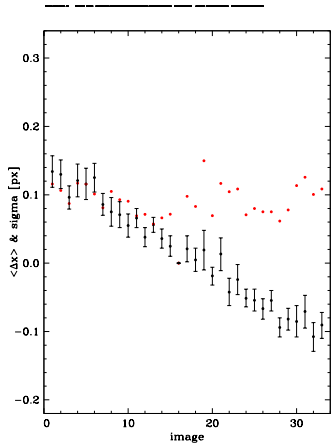

(a) Case (ii): Mean deviation in x position (black) and sigma (red) for images P01 - P33.

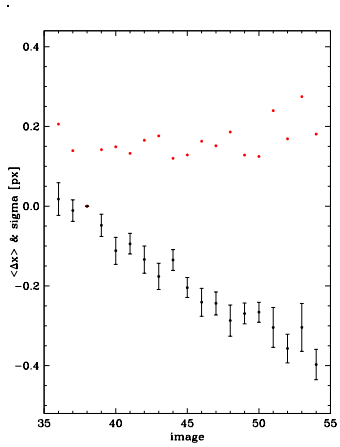

(b) Case (iii): Mean deviation in x position (black) and sigma (red) for images P36 - P54.

Figure 27

(iii) Between 20 and 31 lines were identified. Exposure P38 was taken as reference frame with 31 lines identified, and the standard deviation of the residuals after a successful fit varied between 0.076 and 0.12.

As in case (ii), the mean x-position of the lines decreases with time, see Fig. 27b, while the sigma stays constant. The rate is 0.355 px/hr or 0.118 Å/hr.

As in case (ii), I applied the solution of exposure P38 to all measured x-positions and obtained a rate of 0.119 Å/hr. Finally, Fig. 28b shows the drift of the first parameter in the solution (a_0 in a third order Legendre polynomial) with time, where the rate is 0.084 Å/hr.

Conclusions:

(i)
- The x-position of a line varies with time when the telescope is tracking: on average 0.012 pixel/minute or 0.696 pixel/hour. This corresponds to 0.0026 Å/m or 0.1561 Å/hr.
- The scatter of repeated measurements is constant with time; it is about 0.15 px or 0.0337 Å.
- The variation depends on the x position or wavelength:
  - On CCD1 (blue) the rate is 0.015 px/m or 0.915 px/hr (0.0034 Å/m or 0.2054 Å/hr);
  - On CCD2 the rate is 0.010 px/m or 0.586 px/hr (0.0022 Å/m or 0.1315 Å/hr);
  - On CCD3 (red) the rate is 0.007 px/m or 0.403 px/hr (0.0015 Å/m or 0.0904 Å/hr);

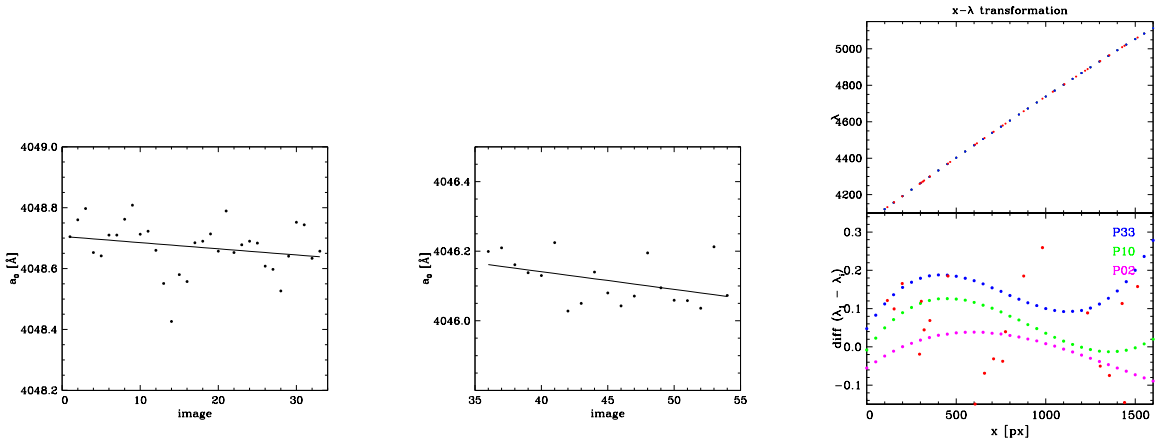

(a) Case (ii): First parameter of the Legendre polynomial solution, a_0, for images P01 - P33.

(b) Case (iii): First parameter of the Legendre polynomial solution, a_0, for images P36 - P54.

(c) Difference in calculated wavelengths between the first image (P01) and images P02, P10 and P33, as indicated.

Figure 28

- There is no variation with the brightness of the line.

(ii) and (iii)

- The x-position of a line varies with time while tracking.
  - The rate depends on the binning;
  - While the rate in case (ii) (20130502) increases, it decreases in case (iii) (20131210) – the same is the case for the tracker x-position.
- Only part of this drift is attributed to the intercept of the Legendre polynomial used in the transformation solution (a_0), the rest is hidden in the other parameters $a_1 - a_3$.

33 MOS stability (Task #60)

Task: To measure repeatability of an observation with the same instrument configuration over time.

Data: Sixteen exposures of the the CuAr lamp were taken continuously until the track ended. The characteristics are:

> 20131116, P01-P16: P001242N06 mask (19 spectra), PG3000 (gr-angle = 43.625, ar-angle = 87.25), filter PC00000, 180s, 2x2 binning, faint/slow.

Data reduction: I have used `specidentify` to overlay the arclamp calibration template CuAr.txt, fitted the data and dumped the x and lambda information of the identified features with 'p' to a file.

Analysis: There are 19 spectra per exposure, identified by their extension number of the extracted

Table 19: Statistics for line identifications per spectrum.

Spectrum (extension) number	Total number of lines	Range of lines identified over all exposures	Reference exposure [Number of lines]	Range of id'd lines [Ångström]	x-position [px]	y-position [px]
01	34	29 – 33	P13 [33]	4228.2 – 4889.0	4466	2080
02	39	30 – 36	P07 [36]	4131.7 – 4806.0	5496	1570
03	35	29 – 34	P10 [34]	4228.2 – 4889.0	4531	1288
04	37	28 – 33	P14 [33]	4103.9 – 4764.9	5656	1372
05	28	24 – 27	P05 [27]	4370.8 – 5017.2	3196	2694
06	36	27 – 34	P09 [34]	4228.2 – 4889.0	4511	1468
07	37	27 – 32	P14 [32]	4198.3 – 4879.9	4771	676
08	37	12 – 31	P05 [31]	4158.6 – 4806.0	5364	3030
09	40	29 – 35	P06 [35]	4131.7 – 4806.0	5526	1990
10	36	26 – 34	P10 [34]	4131.7 – 4806.0	5496	1886
11	34	26 – 32	P09 [32]	4237.2 – 4889.0	4336	2186
12	35	22 – 28	P10 [28]	4052.9 – 4702.3	6549	1790
13	35	28 – 34	P15 [34]	4228.2 – 4889.0	4626	834
14	31	27 – 31	P11 [31]	4300.1 – 4965.1	3796	3158
15	34	29 – 34	P06 [34]	4259.4 – 4933.2	4171	2326
16	36	30 – 35	P04 [35]	4181.9 – 4847.8	5036	3594
17	31	27 – 31	P02 [31]	4277.5 – 4965.1	3976	2556
18	34	26 – 33	P06 [33]	4259.4 – 4933.2	4191	262
19	38	28 – 34	P07 [34]	4158.6 – 4806.0	5206	926

spectrum. The automated spectral identification task does not always identify the same lines in all images, and some lines were rejected as having too large residuals. For the analysis I chose the exposure (per spectrum) with the most lines identified as the reference exposure to calculate line shifts in pixels.

Table 19 gives per spectrum the total number of lines identified, the range of lines identified over all exposures, the exposure used as reference and the number of lines identified in this case, the range of wavelengths across the spectrum (given by the first and last line identified), and the x- and y-position (in case of x one (arbitrary) line was identified and the x-position of it measured for all spectra). The residuals after a successful fit were of the order 0.020 – 0.060.

In case of spectrum/extension 8 the lines became weaker with successive exposures and finally were not present anymore in the last 3 exposures. I haven't checked whether all the line strength varies with exposure (or how they vary across the y-position in a single exposure).

As for the LS stability test (see Sec. 32), I plotted the mean offset in x-position of all lines per spectrum vs exposure (black) and the sigma in red. Figures 29a and 29b show the example of spectrum 1 and 2, respectively. I don't show all spectra here, but the slope is clearly different for each spectrum.

I therefore calculated from the slope the rate of change in Ångström per hour for all spectra and plotted them versus x- and y-position, see Fig. 29c. There is a clear dependence on x-position, and a possible slight dependence on y-position in the sense that spectra close to the centre line show and opposite change to those further towards the edge of the detector.

I also calculated the slope of the change in x-position with time for each individual line (per

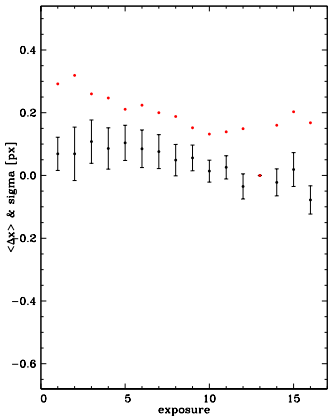

(a) Mean offset in x position (black) and sigma (red) of all lines measured versus exposure number for Spectrum 1.

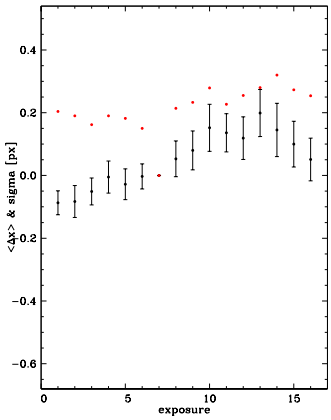

(b) Mean offset in x position (black) and sigma (red) of all lines measured versus exposure number for Spectrum 2.

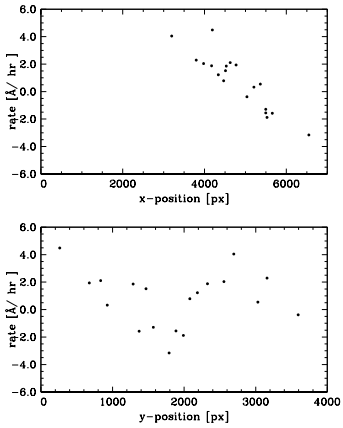

(c) The rate of change in Ångström/hour for all spectra versus x-position (top) and y-position (bottom).

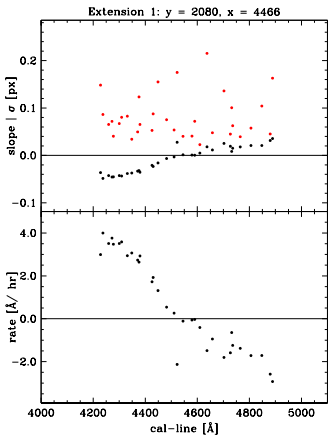

(d) The slope (black; top) and rms (red; top) and the rate of change in Ångström/hour (bottom) for each line of Spectrum 1.

Figure 29

spectrum), the rms for that fit, and the rate of change in Ångström. Figure 29d shows Spectrum 1 as an example. It is clear that the lines shift in different direction across the detector, with the blue lines shifted towards the red (larger x) and the red lines shifted towards the blue (smaller x) across all exposures.

Conclusions:

- The x-position of a line in a spectrum varies with time when the telescope is tracking:
  - The rate can be up to 1 px/hr which corresponds to 4.5 Å/hr.
- Every spectrum has a different rate:
  - This rate depends strongly on the x-position of the slit;
  - For centred slit positions the rate is zero, while bluer spectra show a positive rate and redder spectra show a negative rate.
  - The latter pattern is also present for each individual spectrum when looking at the shift of each spectral line with time.

34 LS and MOS UV capability (Tasks #69 and #70)

Task: To demonstrate fundamental astronomical capability: high near-UV throughput and ability to reduce and calibrate data at the bluest wavelengths.

Data: The same data as for LS_uv and MOS_uv were used:

(i) Three LS-exposures of standard stars were used:

CD-32d9927: P20130820 with P08, 60sec

EG21: P20130826 with P88, 60sec

HILT600: P20131009 with P37, 120sec

The other characteristics are:

PL0400N001 mask, PG3000, (gr-angle = 34.0, ar-angle = 72.25), filter PC00000, 2x2 binning, faint/slow.

(ii) Two MOS observations of the South Galactic Pole region were used. The characteristics are:

20130902, P37 and P38: P001083N03 mask, PG0900 (gr-angle = 12.875, ar-angle = 25.75), PC03200, 664s, 2x2 binning, faint/slow.

Data reduction: I have reduced the spectra using `pysalt`.

(i) Instead of using arc lamp data I used `caltype=rss` for `specrectify`. I extracted the spectra using the following sections:

CD-32d9927: [978:1008]

EG21: [990:1019]

HILT600: [1046:1075]

(ii) I used the ThAr arc lamp observation P39 for calibration. I extracted the spectra of one galaxy and two quasars using the sections listed in Table 7.

Conclusions:

(i) 3 Standard stars (CD-32d9927, EG21, Hilton 600) were observed (under non-photometric conditions) and show a SNR = 50 – 90 in the UV at ∼3000 Ångström and SNR = 100 – 160 at ∼4000 Ångström.

(ii)
- 2 QSOs with a power law spectrum ($\alpha = -1.5$) with R = 19.2 and 19.8 have been detected at SNR = 6 − 17 and 4 − 16, respectively (lower value for UV end).
- One early-type galaxy with R=17.6 was detected at SNR = 5 − 32 (lower value for UV end).

References

Bologna, L.A., Carter, D., 2009, Characterization of the PDET CCD - new gain settings, http://www.saao.ac.za/l̃ab/pdetchar2/index.html

Bologna, L.A., 2011, Anomalous gains of the PDET CCD - 2011 June, http://www.salt.ac.za/l̃ab/pdetanom/index.html

Burgh, E.B., Nordsieck, K.H., Kobulnicky, H.A., ... O'Donoghue, D., (& 3 authors from 3 institutions), 2003, The Prime Focus Imaging Spectrograph for the Southern African Large Telescope: optical design, in Instrument Design and Performance for Optical/Infrared Ground-based Telescopes, SPIE Proc. 4841, p. 1463, eds M. Iye, A.F.M. Moorwood. SPIE, Bellingham, Wa.

Crawford, S.M., 2011, Gain measurements made on 20110622, http://wiki.salt.ac.za/index.php/Gain_measurements_made_on_20110622

Gulbis, A., 2011, Investigation of fringing in RSS narrow band flatfield images, SALT document 2254AA0001, http://wiki.salt.ac.za/index.php/File:SALT.2254AA0001.v2.1.pdf

Gulbis, A., 2013, RSS slotmode timing test, SALT document 2129AA001, http://wiki.salt.ac.za/index.php/File:SALT.2129AA001.pdf

Kniazev, A, 2011, Open-Loop Telescope Tracking, https://wiki.salt.ac.za/index.php/Old_Commissioning_Page#Open-Loop_Telescope_Tracking

Kobulnicky, H.A., Nordsieck, K.H., Burgh, E.B., ... O'Donoghue, D., (& 3 authors from 2 institutions), 2003, The Prime Focus Imaging Spectrograph for the Southern African Large Telescope: operational modes, in Instrument Design and Performance for Optical/Infrared Ground-based Telescopes, SPIE Proc. 4841, p. 1634, eds. M. Iye, A.F.M. Moorwood. SPIE, Bellingham, Wa.

Miszalski, B., 2011, A short analysis of trends in SALTICAM and RSS BIAS frames taken during 2011, http://wiki.salt.ac.za/index.php/File:MiszalskiBiasRep.pdf

Mohan, V. 2011, Flatfielding with SALT, https://sciencewiki.salt.ac.za/index.php/File:Vm_flat_report.pdf

Nordsieck, K., 2012, RSS Sky – Detector transformation, http://wiki.salt.ac.za/index.php/File:Coordtransform_120514.pdf

Pickering, T., 2011, 20110303 pointing analysis, http://wiki.salt.ac.za/index.php/20110303_pointing_analysis

Schröder, A.C., 2013a, RSS Bias analysis, https://sciencewiki.salt.ac.za/index.php/A._Schroeder_RSS_Bias_analysis

Schröder, A.C., 2013b, LS focus further analysis, https://wiki.salt.ac.za/index.php/LS_focus_further_analysis

Väisänen, P., 2014, SALT on-sky throughput, https://wiki.salt.ac.za/index.php/LS_tput_analysis

Väisänen, P., 2013, Dealing with fringing on RSS spectroscopic frames, SALT document, http://wiki.salt.ac.za/index.php/File:SALT_RSS_fringing.pdf

Väisänen, P., 2012, Stability of inserting a MOS mask, http://wiki.salt.ac.za/index.php/ Stability_of_inserting_a_MOS_mask

Väisänen, P., 2011, MOS status October 2011, SALT document (http://wiki.salt.ac.za/index.php/File:MOS_status_oct2011.pdf)

Väisänen, P., Kniazev, A, 2011, RSS efficiency in long-slit mode, SALT document (http://wiki.salt.ac.za/index.php/File:RSS-eff-dec2011.pdf)